Differential Impacts on Host Transcription by ROP and GRA Effectors from the Intracellular Parasite *Toxoplasma gondii*

Suchita Rastogi[1], Yuan Xue[2], Stephen R. Quake[*,2,3,4,#], John C. Boothroyd[*,2,#]

*Equal contribution

[1]Department of Microbiology and Immunology, Stanford University School of Medicine, Stanford, CA, USA

[2]Department of Bioengineering, Stanford University, Stanford, CA, USA

[3]Department of Applied Physics, Stanford University, Stanford, CA, USA

[4]Chan Zuckerberg Biohub, San Francisco, CA, USA

[#]Correspondence should be addressed to J.C.B. (jboothr@stanford.edu) and S.R.Q. (steve@quake-lab.org).

Abstract: 220 words

Importance: 36 words

Text: 7,228 words

Differential Impacts on Host Transcription by ROP and GRA Effectors from the Intracellular Parasite *Toxoplasma gondii*

Suchita Rastogi, Yuan Xue, Stephen R. Quake*, John C. Boothroyd*

* Equal contribution

ABSTRACT

The intracellular parasite *Toxoplasma gondii* employs a vast array of effector proteins from the rhoptry and dense granule organelles to modulate host cell biology; these effectors are known as ROPs and GRAs, respectively. To examine the individual impacts of ROPs and GRAs on host gene expression, we developed a robust, novel protocol to enrich for ultra-pure populations of a naturally occurring and reproducible population of host cells called uninfected-injected (U-I) cells, which *Toxoplasma* injects with ROPs but subsequently fails to invade. We then performed single cell transcriptomic analysis at 1-3 hours post-infection on U-I cells (as well as on uninfected and infected controls) arising from infection with either wild type parasites or parasites lacking the MYR1 protein, which is required for soluble GRAs to cross the parasitophorous vacuole membrane (PVM) and reach the host cell cytosol. Based on comparisons of infected and U-I cells, the host's earliest response to infection appears to be driven primarily by the injected ROPs, which appear to induce immune and cellular stress pathways. These ROP-dependent pro-inflammatory signatures appear to be counteracted by at least some of the MYR1-dependent GRAs and may be enhanced by the MYR-independent GRAs, (which are found embedded within the PVM). Finally,

47 signatures detected in uninfected bystander cells from the infected monolayers
48 suggests that MYR1-dependent paracrine effects also counteract inflammatory ROP-
49 dependent processes.
50
51 **IMPORTANCE**
52 This work performs the first transcriptomic analysis of U-I cells, captures the
53 earliest stage of a host cell's interaction with *Toxoplasma gondii*, and dissects the
54 effects of individual classes of parasite effectors on host cell biology.
55
56 **MAIN TEXT**
57 **Introduction**
58 The obligate intracellular parasite *Toxoplasma gondii* parasitizes a wide range of
59 avian and mammalian organisms, including humans (1). During the acute phase of
60 infection, this unicellular eukaryote rapidly expands within host tissues by penetrating
61 host cells, establishing and replicating within an intracellular parasitophorous vacuole
62 (PV), and simultaneously avoiding clearance by the host immune system (reviewed in
63 (2)). To orchestrate these events (Fig. 1A), *Toxoplasma* employs a vast repertoire of
64 effector proteins housed primarily in two secretory organelles, the rhoptries and dense
65 granules. The rhoptry organelle effectors (ROPs) are secreted by the parasite into the
66 host cytosol during or immediately prior to invasion by an as yet undefined mechanism
67 (reviewed in (3)). The handful of ROPs that have been characterized to date include
68 virulence factors that disrupt immune clearance mechanisms (4-7), remodel the host's
69 cortical actin cytoskeleton at the point of parasite penetration (8, 9), and co-opt the

70 STAT3 and STAT6 pathways (10-12). In contrast, the dense granule effectors (GRAs)
71 are thought to be secreted later during the invasion process and mostly after the
72 parasite has invaded the host cell (reviewed in (3)). Many GRAs remain in the PV lumen
73 or PV membrane (PVM) (13-17), but others traverse the PVM to reach the host cytosol
74 and often proceed to the host nucleus (18-24). The translocation of this latter class of
75 GRAs across the PVM is dependent on a group of PVM proteins called the MYR
76 complex, i.e., MYR1, MYR2, and MYR3, which are so-named because they are
77 required for parasite-dependent host c-Myc regulation (25-27). Host signaling pathways
78 modulated by the PVM-embedded, MYR-independent GRAs (MIGs) include the nuclear
79 factor kappa light chain enhancer of activated B cells (NF-kB) pathway. Host pathways
80 modulated by MYR-dependent GRAs (MDGs) include the interferon gamma (IFN-
81 gamma), mitogen activated protein kinase (MAPK), and p53 pathways, as well as the
82 cyclin E regulatory complex (22, 23, 28).
83 The collective host response to ROPs, MDGs, MIGs, and other perturbations
84 during infection with *Toxoplasma gondii* have been well-documented in transcriptomic
85 studies that compare infected and mock-infected cells; however, the contribution of
86 individual parasite effector compartments to the overall picture is more poorly defined,
87 particularly because many parasite effectors are introduced during the earliest stages of
88 infection in very narrow time intervals. Specifically, invasion is a rapid process that takes
89 approximately 40 seconds (29), and deployment of the ROPs likely occurs during the
90 first third of invasion in one shot (30). In contrast, MDGs have been detected by
91 immunofluorescence assays in the nuclei of parasitized host cells at ~3 hours post-
92 invasion at the earliest (19), which suggests that they likely modulate host transcription

much later than ROPs. Parasite mutants that lack a functional MYR complex have helped separate the impact of MDGs from those of other parasite effectors (25, 26, 31), but the specific impact on host transcription by ROPs and MIGs has yet to be determined. The rhoptry organelle's contribution is of particular interest given that ROP injection is essential to parasite invasion, survival, and virulence, and the functions of most ROPs are unknown.

Here we document the impact of specific classes of parasite effector, including for the first time ROPs, by leveraging a rare population of host cells that parasites inject with ROPs but subsequently fail to invade (32). These uninfected-injected (U-I) host cells (Fig. 1B) do not arise as a result of parasite-derived exosomes delivering effectors to host cells (32) or due to impending host cell death (Fig. 1D). They arise spontaneously in tissue culture and may also arise *in vivo* in the brains of mice chronically infected with *Toxoplasma* (32). To interrogate the host response specifically to effectors injected before invasion, we developed a novel pipeline to purify and perform single cell RNA sequencing (scRNAseq) of U-I cells. To resolve the impact of effectors released during vs. after invasion, we also analyzed U-I cells from infection with parasites lacking MYR1, a component of the complex required for translocation of MDGs into the host cytosol (25, 26). Our findings reveal new insight into the impact of individual parasite effector compartments on the biology of *Toxoplasma*-infected host cells.

116 **Results**

117 ***A Novel FACS-based Strategy Purifies Uninfected-Injected Host Cells for Single***

118 ***Cell RNA Sequencing***

119 To investigate the impact of injected parasite effectors on host biology, we

120 devised a fluorescence activated cell sorting (FACS)-based pipeline that purified U-I

121 cells for transcriptomic analysis (Fig 1C). The pipeline employed the toxofilin-beta-

122 lactamase (Tfn-BLA) assay (8), in which host cell monolayers were: 1) exposed to red

123 fluorescent RH (type I) strain parasites expressing the ROP fusion protein Tfn-BLA, and

124 then 2) stained for 30 minutes with CCF2-AM, a reporter dye that is taken up by live

125 host cells and shifts from green to blue fluorescence when cleaved by BLA. CCF2-AM

126 staining occurred at 30, 90, or 150 minutes post-infection, to yield cells at 1, 2, or 3

127 hours post-infection (hpi; Fig. 1C). U-I cells were then FACS sorted based on their blue

128 CCF2-AM fluorescence and their absent red fluorescence (since they lacked

129 internalized parasites). As experimental controls, we also sorted for infected cells

130 (designated I-I cells for being infected and injected) and uninfected bystander cells

131 (denoted U-U cells for being uninfected and uninjected) from the same host cell

132 monolayer as the U-I cells, as well as for mock-infected cells from a separate monolayer.

133 Single cells and bulk populations of 50-100 cells of each type (e.g., U-I, I-I, etc.) were

134 collected. This strategy enabled transcriptomic assessment of paracrine effects during

135 *Toxoplasma* infection (by comparison of U-U vs. mock-infected cells) and generated

136 pure I-I and U-I cell populations at extremely short infection durations, an improvement

137 over traditional methods that rely on high multiplicities of infection (MOIs) and long

138 infection times to distinguish infected vs. uninfected transcriptomic signatures. We

139 chose 10 T1/2 mouse fibroblasts as the preferred host cell type over conventionally
140 used human foreskin fibroblasts (HFFs), which we found unsuitable for single cell sorts
141 due to their propensity to remain clumped in FACS buffer.

142 To ensure confidence in the identity of the sorted cells and to limit the number of
143 parasites per I-I cell to one, we gated stringently, particularly for the "U-I cells" gate and
144 "parasite-associated" gate (which included I-I cells; Fig. 1D). We also subjected all cells
145 to extensive washes before FACS sorting, as debris from the human feeder cells used
146 to culture the parasites contaminates the U-I gate (Fig. S1), likely due to retention of
147 both CCF2-AM dye and the parasite fusion protein Tfn-BLA. Of note, these posed
148 significant challenges to downstream bioinformatic analyses of bulk U-I cells, but they
149 registered as single cells in the scRNA-seq pipeline and were automatically discarded
150 during quality control due to their high percentage of human reads. At a multiplicity of
151 infection (MOI) of ~6, U-I cells constituted ~8.8% of the injected (i.e., U-I + I-I) cell
152 population at 1 hpi, ~2.0% at 2 hpi, and ~3.4% at 3 hpi (Fig. 1E). Abundances of sorted
153 U-I, I-I, and U-U cells relative to all sorted cells are depicted in Fig. 1F.

154 To validate U-I cells as appropriate models for host responses to injected
155 parasite effectors, we also limited the possibility of U-I cells arising by mechanisms
156 other than aborted invasion events. One such mechanism is host immune clearance of
157 internalized parasites. However, this route is an unlikely source of U-I cells in our
158 pipeline for two reasons: 1) immune clearance of intracellular pathogens in mouse cells
159 is activated by exogenous IFN-gamma, which we did not add to the host cells, and 2) all
160 known strains of *Toxoplasma* escape IFN-gamma-mediated pathogen clearance by
161 suppressing the IFN-gamma signaling pathway if they infect the host cell before it is

162 exposed to extracellular IFN-gamma (33, 34). In another potential mechanism, an
163 infected host cell may divide and produce an uninfected daughter (a U-Id cell, for U-I by
164 division). To limit the occurrence of U-Id cells, we serum starved all host cells for the 24
165 hours preceding infection to induce cell cycle arrest (Fig. S2A) and limited infection
166 durations to 3 hpi or less, as live video microscopy of 200 parasite-infected, serum-
167 starved 10 T1/2 host cells for 16 hours revealed that no infected cell divided before 3.67
168 hpi (Fig. S2B). Finally, a newly internalized parasite might spontaneously exit early from
169 the host cell, a rare and poorly characterized process that is therefore difficult to control.
170 Though we cannot exclude the possibility that a very small number of our U-I cells arose
171 from this mechanism of premature parasite egress, and though U-Id production cannot
172 be completely ruled out, an advantage of scRNA-seq is its ability to distinguish
173 differences between cells arising via different mechanisms (assuming they differ
174 transcriptomically).
175

176 ***Technical Validation of Single Cell Sequencing for Cells Exposed to or***
177 ***Parasitized by* Toxoplasma gondii**

178 Given the limited duration of infection (≤ 3 hours), we expected relatively subtle
179 transcriptional changes in U-I and I-I cells. To maximize the sensitivity of scRNAseq
180 analyses to detect such signatures, we employed Smart-seq2 library preparation and
181 sequenced to a depth of 1 million reads per cell. All reads were aligned to a
182 concatenated mouse-*Toxoplasma* genome using the genomic sequence for the GT1
183 parasite strain, a clonal relative of RH (35, 36). In addition, we identified and discarded

184 47 mouse genes to which reads from extracellular RH parasites aligned (mostly
185 representing evolutionarily conserved genes; Table S1).
186 To ensure that poorly amplified or poorly sequenced host cells did not confound
187 downstream analysis, we filtered samples based on several quality metrics (Materials
188 and Methods), yielding 453, 2,026, and 2,875 cells at 1, 2, and 3 hpi, respectively, for
189 downstream analysis (Fig. S3A). Mapping efficiency of the analyzed cells was >85% in
190 all experimental trials (Fig. S3B). Characterization of measurement sensitivity based on
191 logistic regression modeling of ERCC spike-in standards revealed a 50% detection rate
192 of 31, 11, and 34 RNA molecules per cell at 1 hpi, 2 hpi, and 3 hpi, respectively (Fig.
193 S3C), amounting to a level of sensitivity comparable to that previously reported (37).
194 After filtering out genes with expression above the detection limit in <6 cells, we
195 normalized for sequencing depth across cells by dividing each read count by the
196 median read sum to yield counts in units of “counts per median” (cpm) (Materials and
197 Methods). Gene expression in the single cell RNA-seq dataset exhibited a strong
198 positive correlation to expression in bulk RNA-seq samples processed the same way
199 specifically for differentially expressed genes (DEGs) between experimental conditions
200 (i.e., U-U, I-I, and U-I cells) (Fig. S3D). Furthermore, each bulk experiment’s expression
201 data exhibited the best correlation with their cognate single cell data (Fig. S3E). Taken
202 together, these data demonstrate that scRNAseq captures similar transcriptomic
203 signatures in host cells to those detected in bulk RNA-seq experiments, validating the
204 scRNAseq platform as an approach to further characterize host cell transcriptomic
205 responses during *Toxoplasma* infection.
206

207 ***Single Cell Resolution Reveals Cell-to-Cell Heterogeneity Inaccessible to the Bulk***
208 ***RNA Sequencing Platform***

209 A key advantage of single cell resolution is that it enables identification and
210 separation of parasite-independent host cell heterogeneity. Accordingly, single cell
211 resolution facilitates an extra checkpoint to validate the identities of U-I, I-I and U-U cells
212 by quantifying the percentage of *Toxoplasma*-derived reads in each cell. As expected,
213 *Toxoplasma* read content across all cells exhibited a bimodal distribution, where most
214 uninfected cells contained <0.01% *Toxoplasma* reads, while most infected cells
215 possessed higher, 0.5-4%, percentages. However, a small proportion of U-I cells and I-I
216 cells exhibited unexpectedly high (for U-I) or low (for I-I) *Toxoplasma* read counts and
217 were considered to be misclassified (Fig. S4A). This may have resulted from a low rate
218 of TdTomato or mCherry loss in some of the parasites (for cells misclassified as U-I) or
219 from attached but not fully invaded parasites being dislodged from the host cell at some
220 point between fluorescence detection and deposition of the cell into lysis buffer (for cells
221 misclassified as I-I). Such misclassified cells may have contributed significant and
222 potentially misleading signatures to their respective samples. To preclude this possibility
223 in our single cell dataset, we excluded all U-I cells with >0.04% *Toxoplasma* reads and
224 all I-I cells with <0.32% *Toxoplasma* reads from downstream analysis.

225 Next, because the experimental pipeline examined cells during their earliest
226 interaction with *Toxoplasma*, we expected the subtle, parasite-dependent transcriptional
227 signatures to be potentially eclipsed by intrinsic host processes such as cell cycle,
228 which still progressed in some cells even with serum starvation (Fig. S2A). To separate
229 host cell cycle from other biological processes the parasites could potentially modulate,

230 we determined the phases of all single cells (i.e., G1, S, or G2/M) based on expression
231 of 175 curated cell cycle marker genes (Fig. S4B; Table S2; Materials and Methods). A
232 breakdown of cell cycle phase composition for each experimental condition across all
233 time points revealed a consistent pattern at 2 hpi in which the proportion of cells in G2
234 or M phase increased in a manner that appeared dependent on injected effectors, i.e.,
235 from 13.3% in Mock to 33.9% in Wt U-I, 41.4% in Dmyr1 U-I, and 22.5% in CytD U-I
236 (Fig. S4C). These findings are consistent with potential induction of cell cycle arrest in
237 U-I cells by injected effectors, as previously reported (38-41).

238 To identify other sources of heterogeneity in the dataset, we used the *Uniform*
239 *Manifold Approximation and Projection* (UMAP) algorithm for dimensionality reduction
240 and to visualize relationships between all cells based on the most dispersed (i.e.,
241 variable) genes. Leiden clustering revealed three distinct clusters, designated herein as
242 populations 1, 2, and 3 (Fig. S4D). Curiously, cells from different time points exhibited
243 differences in the proportion of cells belonging to each population, where 2 hpi cells fell
244 entirely in population 1, and 3 hpi cells fell in all three populations. In conventional single
245 cell analysis, dimensionality reduction and cell clustering are used to identify novel cell
246 types. Though the 10 T1/2 cell line is clonal, it is derived from a pluripotent stem cell
247 population which has a propensity to differentiate, such that the three identified
248 populations could conceivably represent distinct differentiation states (42).

249 To limit cell-to-cell heterogeneity from overshadowing potentially subtle
250 transcriptomic signatures induced by parasite effector secretion and parasite invasion,
251 we limited our remaining analyses to host cells in G1 phase (to limit cell cycle
252 signatures) and from UMAP population 1 (to factor out potential cell type signatures).

253

254 ***Injected Parasite Effectors Drive Inflammatory Transcriptional Signatures***

255 ***Associated with Parasite Infection***

256 To determine host responses to ROP and GRA secretion into host cells, we used
257 the Model-based Analysis of Single Cell Transcriptomics (MAST) algorithm to perform
258 differential gene expression analysis on G1 phase, UMAP population 1 cells. Across all
259 pairwise comparisons between conditions within each time point, 39, 2,252, and 10,995
260 differentially expressed genes (DEGs) were detected at 1 hpi, 2 hpi, and 3 hpi,
261 respectively (Table S3A). These results show that parasite effectors and invasion result
262 in almost no detectable transcriptional response at 1 hpi, a modest response involving
263 regulation of a core group of genes at 2 hpi, and ramping up of this response at 3 hpi in
264 which transcription in a much larger set of host cells is modulated. Because of the
265 negligible response at 1 hpi, we excluded data from this time point from the remaining
266 analyses.

267 For additional validation, we assessed the 2 hpi and 3 hpi datasets for their
268 agreement with two previous bulk RNA-seq studies that captured the host response to
269 infection at 6 hpi in nominally the same parasite strains and culture conditions, albeit in
270 HFFs instead of mouse 10 T1/2 fibroblasts (10, 31). Because these studies measured
271 the infection response by comparing infected vs. mock-infected cells, we examined
272 DEGs between Wt I-I and mock-infected (i.e., Mock) cells in our own datasets. Gene set
273 enrichment analysis (GSEA) of the resulting DEGs at 2 hpi and 3 hpi (Table S3B) using
274 the Molecular Signatures Database's Hallmark gene sets (43) revealed that nearly all
275 significantly enriched gene sets at 2 hpi and 3 hpi were previously identified in the Naor

276 et al reference dataset, and many pertained to immune processes (Fig. 2) (31). Of note,
277 gene sets were considered to be significantly enriched if their false discovery rates
278 (FDR) were < 0.25, a standard cutoff for GSEA given the lack of coherence in most
279 transcriptional datasets and the relatively low number of gene sets being analyzed.
280 Nearly all gene sets *not* preserved in the Naor et al reference were enriched from genes
281 *down*regulated upon infection. The lack of agreement between our downregulated gene
282 sets and those obtained from the references likely reflects the infection response's
283 tendency towards gene *up*regulation, and to stochasticity in expression levels for the
284 substantially fewer downregulated genes detected, an interpretation corroborated by the
285 downregulated genes' higher p-values and lower fold changes. Overall these results
286 indicate that the 2 hpi and 3 hpi datasets capture well-known host responses to infection
287 with *Toxoplasma gondii*.
288 Next, to determine the host response to injection of parasite effectors, we
289 compared Wt U-I cells to Wt U-U cells. At 2 hpi, only 10 DEGs were identified (Table
290 S3C), and GSEA of these DEGs revealed no significant enrichment of the Hallmark
291 gene sets. Therefore, injection of parasite effectors without invasion appears to elicit
292 only a trace response at 2 hpi. At 3 hpi, 156 DEGs were detected between Wt U-I and
293 Wt U-U cells (Table S3C), for which GSEA revealed at total of 17 gene sets (Fig. 3A);
294 14 corresponded to genes expressed higher in Wt U-I cells than in Wt U-U cells, and
295 several were associated with inflammation. In addition, 10 gene sets were common to
296 the infection response (Fig. 3B), i.e., also enriched in Wt I-I vs. Mock DEGs, which
297 suggests that much of the early response to parasite infection is driven by the injection
298 of parasite effectors (likely ROPs) into host cells prior to invasion.

299 To confirm that the transcriptional signatures in Wt U-I cells originated from ROP
300 injection, we made two additional comparisons. For the first, we constructed red
301 fluorescent RH *Δmyr1* Tfn-BLA parasites from an RH *Δmyr1* mCherry parental strain
302 ((25); Fig. S5) and used them to infected host monolayers, from which we collected U-U,
303 U-I, and I-I cells. From here on, we designate these mutant parasites as *Δmyr1*
304 parasites and host cells arising from infection with *Δmyr1* parasites as Dmyr1 cells. As
305 MDGs fail to traverse the PVM during *Δmyr1* parasite infections, the absence of MYR1
306 should effectively limit the parasites' effector repertoire to ROPs and MIGs;
307 consequently, transcriptional signatures from U-I cells arising from *Δmyr1* infection (i.e.,
308 Dmyr1 U-I cells) and from wild type infection (i.e., Wt U-I cells) should largely resemble
309 one another. To test this hypothesis, we compared Dmyr1 U-I and Dmyr1 U-U cells. In
310 the second comparison, to account for the possibility that Wt U-I signatures originated
311 from a pre-existing difference in those host cells from their neighbors, rather than from
312 injected effectors, we collected U-U, U-I, and I-I cells from host monolayers exposed to
313 wild type parasites pre-treated with the invasion inhibitor cytochalasin D, which allows
314 parasite attachment but blocks subsequent invasion. As expected, cytochalasin D
315 treatment increased the proportion of U-I cells in infected monolayers by ~6-fold at 2 hpi
316 and by ~9.3-fold at 3 hpi (Fig. S6), so at least 85-90% of the artificially induced U-I cells
317 (i.e., CytD U-I cells) presumably arose from drug-induced abortion of parasite invasion
318 events, rather than from parasite-independent host cell differences. We predicted that
319 transcriptional signatures detected in CytD U-I cells would be driven almost entirely by
320 injected parasite effectors and would mirror those identified in both Wt U-I and Dmyr1
321 U-I cells. As expected, at 2 hpi very few DEGs (29 and 51, respectively) and no

322 enriched gene sets were identified for Dmyr1 and CytD U-I cells vs. their corresponding
323 U-U cells, while at 3 hpi substantially more DEGs (103 and 174 for Dmyr1 and CytD U-I
324 vs. U-U cells, respectively) and gene sets were identified (Table S3D, Table S3E). The
325 3 hpi gene sets exhibited a strong degree of overlap with the original Wt U-I vs. Wt U-U
326 comparison, such that 14 of the 17 Wt U-I vs. Wt U-U gene sets were also identified in
327 either or both of the corresponding Dmyr1 and CytD comparisons (Fig. 3B). These data
328 are consistent with an inflammatory response to ROP injection that drives much of the
329 host cell's total response to parasite infection.

330 In light of the many shared genes and gene sets between the infection vs.
331 injection responses, we sought to define the distinction between these responses by
332 comparing Wt U-I (injected) to Wt I-I (infected) cells using two complementary
333 approaches. In the first approach, we used MAST to identify DEGs between Wt U-I and
334 Wt I-I cells and subjected the DEGs to GSEA. To better compare the trajectories of Wt
335 I-I and Wt U-I gene expression, we also computed fold changes in DEG expression
336 between each of these conditions and Wt U-U cells (Table S3F). In the second
337 approach, we identified genes with significant differences between Wt U-I and Wt I-I
338 cells in their correlation to a quantity called the CCF2-AM ratio, i.e., the ratio of blue
339 (cleaved) to green (uncleaved) CCF2-AM indicator dye detected during FACS sorting.
340 Briefly, the CCF2-AM ratio is a biological readout for penetration of a host cell by
341 injected ROPs. We identified genes that exhibited significant shifts between Wt U-I and
342 Wt I-I cells in their relationship to the CCF2-AM ratio (Table S4A) by first modeling a
343 Gaussian distribution of their Spearman correlations to the CCF2-AM ratio. Next, low
344 probability genes with a sufficient difference in their CCF2-AM correlation scores in Wt

345 U-I vs. Wt I-I cells were interpreted to be associated with either ROP injection alone (in
346 Wt U-I cells) or with all secreted effectors plus parasites (in Wt I-I cells, in which ROP
347 penetration should be accompanied by all other parasite-induced insults).

348 Analysis of Wt I-I vs. Wt U-I cells at 2 hpi revealed no significant DEGs, pointing
349 to a profound similarity in host transcription in Wt I-I and Wt U-I cells at 2 hpi. However,
350 the corresponding CCF2-AM correlation exhibited a higher sensitivity for detecting
351 differences between Wt I-I vs. Wt U-I cells and yielded 81 significant deviants from the
352 Gaussian distribution (Fig. 4B, top row). Of the deviants, 73 (~90.1%) fell in regions of
353 the scatterplot designated as “counterbalanced,” where the genes were either: 1)
354 negatively correlated with the CCF2-AM ratio in one condition and positively correlated
355 in the other; or 2) had stronger positive or negative correlations in Wt U-I cells than in
356 Wt I-I cells as determined by a Gaussian model (Fig. 4B, top right panel; Table S4A).
357 This provides evidence for downstream events in infection (i.e., release of GRAs,
358 parasite penetration) suppressing effects of genes induced by ROP injection as early as
359 2 hpi.

360 At 3 hpi, 122 DEGs and 423 CCF2-AM correlation deviants were identified for Wt
361 I-I vs. Wt U-I cells, pointing to a divergence in the injection vs. infection responses at
362 this later time point. Of the DEGs, 100 (~82.0%) exhibited opposing trajectories in Wt I-I
363 vs. Wt U-I cells (Table S3F), i.e., they were either: 1) upregulated in one cell type and
364 downregulated in the other compared to a common Wt U-U standard; or 2) more
365 upregulated or downregulated in Wt U-I cells compared to the standard than in Wt I-I
366 cells. In addition, of the CCF2-AM correlation deviants, 333 (~79%) exhibited at least a
367 moderate negative correlation with the CCF2-AM ratio in Wt I-I cells, an observation

368 consistent with these genes being downregulated in response to the combination of all
369 parasite-derived insults and effectors during infection (Fig. 4A, bottom left panel; Table
370 S4A). Furthermore, 282 (~67%) of the deviants fell in regions of the scatterplot
371 designated as “counterbalanced” (Fig. 4A, bottom right panel; Table S4A), which is
372 consistent with host responses in Wt U-I cells being counteracted by parasite effectors
373 that are operating in Wt I-I cells only. This lends further support to the notion that
374 effectors injected circa invasion (i.e., ROPs) are counterbalanced by subsequently
375 introduced effectors (i.e., GRAs). Of note, the remaining 141 CCF2-AM deviant genes
376 at 3 hpi fell within the “enhanced” sections of the scatterplot (Fig. 4A, bottom right panel;
377 Table S4A). This suggests that while GRA release and parasite penetration may
378 counterbalance some ROP-induced host responses, these events may also enhance
379 other genes induced by ROP injection.

380 To discern the biological significance of the differences between the infection vs.
381 injection responses, we performed GSEA on Wt U-I vs. Wt I-I DEGs. The resulting
382 enriched gene sets included many that were previously identified in the host infection
383 response, with gene sets enriched from genes expressed higher in Wt I-I cells
384 corresponding to more inflammatory processes (Fig. 4B). Because the vast majority of
385 genes with higher expression in Wt U-I cells than in Wt I-I cells exhibited evidence of
386 being counterbalanced (84 out of 93 genes; Table S3F), these findings are consistent
387 with injection-associated inflammatory host processes ramping up upon parasite
388 penetration (and GRA release), while other injection-associated processes are
389 dampened by these later events.
390

391 ***Parasite Effectors Counterbalance to Yield a Modest Host Response to Early***
392 ***Parasite Infection***

393 Next, we sought to determine the contribution of individual parasite effector
394 compartments to the difference between the host infection (in Wt I-I cells) vs. ROP
395 injection (in Wt U-I cells) responses. According to the current model of parasite effector
396 secretion (Fig. 1A), the host response to an infection with *Toxoplasma* tachyzoites can
397 be attributed to 5 parasite-dependent stimuli: 1) secretion of paracrine effectors into the
398 extracellular milieu; 2) injection of ROPs; 3) activity of MIGs; 4) secretion of MDGs; and
399 5) parasite invasion and establishment of the PV (Table 1). Because Wt U-I and Wt I-I
400 cells are both injected with ROPs and originate from the same monolayer, ROPs and
401 paracrine effectors likely do not explain the differences between these two cell types.
402 Instead, MDGs, MIGs, and the act of parasite penetration itself are, *a priori,* most likely
403 to explain these differences. Our dataset, which includes infected (I-I), bystander
404 uninfected (U-U), and U-I cells originating from monolayers infected with wild type and
405 *Δmyr1* parasites, presents a unique opportunity to examine the impacts of these
406 compartments in isolation.

407 To determine how individual effector compartments contribute to the
408 transcriptomic differences between Wt I-I vs. Wt U-I cells, we made two key
409 comparisons. In the first comparison, we examined Dmyr1 U-I cells, which presumably
410 respond to ROP injection, and Dmyr1 I-I cells, which are thought to respond to ROP
411 injection plus MIGs and parasite penetration (Table 1). We predicted that MIGs and
412 parasite penetration would account for the differences between Dmyr1 I-I and Dmyr1 U-
413 I cells, and for a subset of the differences between Wt U-I and Wt I-I cells. In the second

414 comparison, we examined Wt I-I vs. Dmyr1 I-I cells, which originate from monolayers
415 infected with wild type and *Δmyr1* parasites, respectively. Signatures detected in Dmyr1
416 I-I cells likely reflect the host response to the combination of ROP injection, MIG activity,
417 parasite penetration of host cells, and paracrine effectors secreted into the extracellular
418 milieu, while those detected in Wt I-I cells likely reflect the response to these elements
419 plus MDG secretion (Table 1). Therefore, we predicted that comparing Dmyr1 I-I vs. Wt
420 I-I would illustrate the impact of MDGs, as well as any paracrine effects dependent on
421 the presence of MYR1, and that this would account for a second subset of the
422 differences between the infection vs. injection response showcased in the Wt I-I vs. Wt
423 U-I comparison.
424
425 *MYR-Independent GRAs and Parasite Penetration Collectively Enhance ROP-induced*
426 *Inflammatory Responses*
427 To examine the host response to the combination of MIGs and parasite
428 penetration, we compared Dmyr1 U-I cells, which should be penetrated by ROPs, and
429 Dmyr1 I-I cells, into which parasites should secrete ROPs and MIGs, but not MDGs
430 (Table 1; Table S3G). At 2 hpi, only 5 DEGs and no GSEA enriched gene sets were
431 identified, implying profound similarity between Dmyr1 U-I and Dmyr1 I-I cells at this
432 time point (also the case for Wt U-I vs. Wt I-I cells). At 3 hpi, 80 DEGs were identified,
433 pointing to a slight divergence between these two cell types at this time point. 48 (60%)
434 of the DEGs exhibited evidence of counterbalancing (i.e., their expression exhibited
435 either: 1) opposing trends in Dmyr1 U-I vs. Dmyr1 I-I cells when compared to an
436 uninfected Dmyr1 U-U standard; or 2) a stronger induction or suppression in Dmyr1 U-I

437 cells than in Dmyr1 I-I cells), which suggests that MIGs may play a role in neutralizing
438 the effects of the ROPs preceding them. Note, however, that we cannot exclude the
439 possibility that this effect is attributable to stimuli related to physical penetration by the
440 parasites. GSEA of the 3 hpi DEGs identified 15 enriched gene sets (Fig. 5), of which 9
441 were also found to be enriched in the Wt U-I vs. Wt I-I comparison. For gene sets
442 enriched from genes expressed higher in Dmyr1 I-I cells than in Dmyr1 U-I cells, many
443 corresponded to gene sets already identified as part of the host response to ROP
444 injection and/or were associated with inflammatory processes. In contrast, none of the
445 gene sets enriched from genes expressed higher in Dmyr1 U-I cells were identified as
446 part of the injection response. Taken together, these results suggest that MIGs and
447 parasite penetration do indeed account for much of the difference between the infection
448 response (in Wt I-I cells) vs. the injection response (in Wt U-I cells). More specifically,
449 inflammatory processes associated with ROP injection appear to be enhanced by the
450 combination of MIGs and parasite penetration, while other processes (i.e., complement
451 cascade, coagulation, MTORC1 signaling, and myogenesis) are suppressed.
452
453 *MYR-dependent GRAs Counterbalance Parasite Effectors Released Earlier in the Lytic*
454 *Cycle*
455 A previously published bulk RNA-seq experiment comparing host transcription in
456 monolayers infected with wild type vs. *Δmyr1* parasites at 6 hpi (31) revealed a set of
457 genes such that in the absence of MYR1, expression changes were unmasked, while in
458 the presence of MYR1 (i.e., during wild type infection), there was no net change. This
459 work implies that collectively, MDGs and associated paracrine effectors secreted during

460 infection with wild type but not *Δmyr1* parasites participate in counterbalancing
461 transcriptional signatures induced by prior parasite-dependent stimuli.
462 To determine whether MDGs and associated paracrine effects play a similar role
463 in the present single cell datasets, and to ascertain their contribution to the difference
464 between the infection vs. injection responses, we compared Dmyr1 I-I and Wt I-I cells.
465 MAST analysis of this comparison identified 46 and 367 DEGs at 2 hpi and 3 hpi (Table
466 S3H), respectively. While GSEA of the 2 hpi DEGs returned no significantly enriched
467 gene sets, GSEA at 3 hpi revealed 16 significantly enriched gene sets, of which all but
468 one were enriched from genes expressed higher in Dmyr1 I-I cells than in Wt I-I cells.
469 Furthermore, 8 gene sets were identified in the previously published bulk RNA-seq
470 experiment comparing infections with wild type vs. *Δmyr1* parasites (31), while 6
471 corresponded to infection-associated gene sets (i.e., were enriched from Wt I-I vs. Mock
472 DEGs), and 8 were identified as part of the ROP injection response (i.e., were enriched
473 from Wt U-I vs. Wt U-U DEGs) (Fig. 6A). Taken together, these data are consistent with
474 MDGs and/or their associated paracrine effects selectively impinging on Wt I-I cells and
475 dampening the effects of parasite effectors introduced into host cells earlier in the lytic
476 cycle. The overlap between these gene sets and those of the injection response shows
477 that some of the counterbalanced effectors include injected effectors (i.e., ROPs), which
478 was previously suspected (31) but never before explicitly demonstrated.
479 Though comparing Dmyr1 I-I vs. Wt I-I cells illustrates the collective impact of
480 MDGs and MYR-dependent paracrine effects on host transcription (Table 1), this
481 comparison cannot distinguish the individual impacts of these two stimuli. To determine
482 the effect of MDGs alone, we performed CCF2-AM ratio correlation analysis on Wt I-I vs.

483 Dmyr1 I-I cells (Table S4B), as was performed for Wt I-I vs. Wt U-I. This type of analysis
484 excludes the impact of paracrine effects because each set of CCF2-AM ratios results
485 from a comparison of I-I cells to U-U cells from the same infected monolayer, rather
486 than to mock-infected cells from a separate monolayer. 224 and 343 CCF2-AM ratio
487 correlation deviants were identified between Wt I-I and Dmyr1 I-I cells at 2 hpi and 3 hpi,
488 respectively. 218 (~97.3%) and 297 (~86.6%) deviants at 2 hpi and 3 hpi, respectively,
489 fell in the "counterbalanced" parts of the CCF2-AM correlation scatterplot (Fig. 6B;
490 Table S4B), which implies that signatures induced by effectors released into Dmyr1 I-I
491 cells are dampened specifically by MYR-dependent effectors released into Wt I-I cells.
492

493 *MYR-dependent Paracrine Effects Also Counterbalance Parasite Effectors Released*
494 *Earlier in the Lytic Cycle*

495 To determine the impact of specifically paracrine factors on the host response,
496 we examined two key comparisons: Wt U-U vs. Mock (which captures all paracrine
497 effects; Table S3I) and Dmyr1 U-U vs. Mock (which captures MYR-independent
498 paracrine effects; Table S3J). Differences between these two comparisons should be
499 attributable to paracrine factors released from host cells in a MYR-dependent fashion.
500 At both 2 hpi and 3 hpi, paracrine effects exhibited robust differences between
501 wild type vs. *Δmyr1* parasite infections. At 2 hpi, ~196 and 54 DEGs were identified for
502 the Dmyr1 and Wt cell comparisons, respectively; at 3 hpi, the difference was even
503 more pronounced, with 1864 DEGS identified for the Dmyr1 comparison vs. only 20
504 DEGs for Wt. GSEA of Dmyr1 U-U vs. Mock DEGs exposed an abundance of gene sets,
505 many of which corresponded to inflammatory processes and other pathways found to

506 be part of the infection response, whereas GSEA of Wt U-U vs. Mock DEGs enriched
507 for few, if any gene sets (3 and 0 at 2 hpi and 3 hpi, respectively) (Fig. 7A). Furthermore,
508 the responses of these DEGs were reproduced consistently between not only U-U cells
509 vs. mock-infected cells, but also between U-I or I-I cells vs. mock-infected cells, which
510 establishes that these trends affect all cell types within a given infected monolayer (Fig
511 7B). Taken together, these results suggest that a MYR-dependent paracrine
512 mechanism suppresses expression of genes induced during *Toxoplasma* infection,
513 including genes belonging to pathways that respond to injected ROPs.
514

515 ***Model of Host Responses to Individual* Toxoplasma *Parasite-Dependent Stimuli***
516 ***and Effector Compartments***

517 The preceding analyses have accounted for host responses to 6 parasite-
518 dependent stimuli: ROP injection, MIGs, MDGs, MYR-independent paracrine effects,
519 MYR-dependent paracrine effects, and parasite invasion. To succinctly represent the
520 interplay between these stimuli, we curated a list of gene sets that best represented the
521 expression trends captured in our analyses. Gene sets were included if they were
522 significantly enriched (FDR < 0.25) from DEGs between a majority of the following 8 key
523 comparisons: 1) Wt U-I vs. Wt U-U (ROP injection); 2) Wt I-I vs. Dmyr1 I-I (MDGs +
524 MYR-dependent paracrine effects); 3) Wt U-U vs. Dmyr1 U-U (MYR-dependent
525 paracrine effects); 4) Dmyr1 I-I vs. Dmyr1 U-I (MIGs + parasite invasion); 5) Dmyr1 U-U
526 vs. Mock (MYR-independent paracrine effects); 6) Wt I-I vs. Wt U-I (MIGs + MDGs +
527 parasite invasion); 7) Wt I-I vs. Wt U-U (all stimuli except paracrine effects); and 8) Wt I-
528 I vs. Mock (all stimuli). The 12 gene sets selected included those pertaining to immune

529 responses, cell proliferation, cellular stress, and the complement pathway. Expression
530 trends for the DEGs within these gene sets are summarized in Fig. 8.
531 Based on our analyses, we propose the following model of parasite-driven effects
532 on host cell transcription. First, because Wt U-I cells appeared to induce DEGs in nearly
533 all the showcased gene sets compared to Wt U-U cells, ROP injection likely induces
534 many of the pathways these gene sets capture, particularly immune-related and cellular
535 stress pathways (Fig. 8A and Fig. 8B, ROPs; Fig. 8C, ROP injection). These signatures
536 may arise in response to the ROPs themselves, or due to cell trauma secondary to
537 perforation of the host cell membrane by the parasite during ROP injection. Next,
538 parasites penetrate the host cell and secrete MIGs into the PVM. The host response to
539 these two stimuli together is relatively mild, as evidenced by the high FDRs and small
540 number of genes per gene set, even at 3 hpi. Though MIGs + Parasites appeared to
541 counterbalance the effects of ROP injection at the gene level, their most significant
542 impact at the gene set level appears to be enhancement of inflammatory transcriptional
543 signatures induced by ROP injection (Fig. 8A and Fig. 8B, MIGs + Invasion; Fig. 8C,
544 MIG Secretion and Parasite Penetration). This does not exclude the possibility that
545 other host processes not covered by the Hallmark gene sets are suppressed by MIGs +
546 Parasites. Next, in cells infected with *Δmyr1* parasites, MYR-independent paracrine
547 factors secreted by neighboring infected cells appear to enhance the effects of ROP
548 injection even more so than MIGs + Parasites and may do so not only for immune-
549 related genes, but also for genes pertaining to cellular stress, complement, and cellular
550 proliferation (Fig. 8A and 8B, dmyr1UU-mock/P(MI)). In contrast, during wild type
551 infections, two additional parasite-dependent stimuli, MDGs and MYR-dependent

552 paracrine factors, both appear to rein in transcriptional signatures induced by the other
553 stimuli (Fig. 8A and 8B, MDGs + P(MD); Fig. 8C, MYR-dependent stimuli), with MYR-
554 dependent paracrine factors (Fig. 8A and 8B, MDGs + P(MD)) and MDGs (Fig. 6B)
555 each contributing a significant counterbalancing effect in their own right. Together, all
556 six parasite classes produce transcriptional signatures that veer toward induction of
557 genes pertaining to inflammation and cellular stress but that are less pronounced than
558 the response to injection of ROPs.
559

560 **Discussion**

561 In this study, we examined host responses to infection with the parasite
562 *Toxoplasma gondii* using scRNA-seq on *in vitro* uninfected-injected (U-I) host cells,
563 which arise from aborted invasion events and that have until very recently (44) been
564 characterized primarily morphologically. Key fixtures of our experimental pipeline
565 included: 1) early time points, to limit isolating false positive U-I cells arising from
566 mechanisms besides aborted invasion; 2) FACS sorts, which purified rare U-I cells and
567 relatively rare infected cells at early time points; and 3) single cell resolution, which
568 enabled bioinformatic validation of all cells' infection status. The level of confidence lent
569 by these measures to the validity of the captured U-I cells enabled interrogation of host
570 responses specifically to ROP injection, an aspect of parasite infection previously
571 inaccessible to study due to the rapid kinetics of effector secretion at the time of
572 invasion. Note that while others have also used scRNA-seq to measure host responses
573 to *Toxoplasma* infection at a single cell level, these studies analyzed cells from animals

574 at many days post-infection, and therefore did not assess the earliest impacts of
575 infection or particularly ROP injection (45).
576 Because the experimental pipeline also leveraged infections with *Δmyr1*
577 parasites, our dataset is a comprehensive resource for the individual impacts of not only
578 ROPs, but also MIGs, MDGs, and paracrine stimuli on host transcription. Our analyses
579 revealed an early response to *Toxoplasma* infection with subtle yet clear signatures
580 overlapping with inflammatory and cellular stress signaling axes. Induction of these
581 axes appears to be 1) driven primarily by ROP injection; 2) enhanced somewhat by the
582 combination of MIGs, parasites, and MYR-independent paracrine factors; and 3)
583 counterbalanced by MDGs and downstream paracrine effects, i.e., factors secreted
584 during wild type but not *Δmyr1* infection. These findings substantiate previous evidence
585 that at least some MDGs suppress host responses induced by other parasite-driven
586 transcriptomic perturbations (31). They may also explain the recent finding that the
587 avirulent phenotype of *Δmyr1* parasites during *in vivo* mouse infections is rescuable by
588 co-infecting animals with both wild type and MYR1-deficient parasites (46); parasites
589 expressing MYR1 may induce host cells to secrete paracrine factors that suppress
590 transcription of inflammatory gene products that would otherwise limit *Δmyr1* parasite
591 infections. Note that while this manuscript was in preparation, a transcriptomic study of
592 U-I macrophages was published by Hunter and colleagues (44). While they used
593 different strains (Pru and CEP), looked at later time points (20-24 hpi), and did not look
594 at MYR1-dependent effects, their primary conclusions that U-I cells experience a major
595 impact of rhoptry effectors (in their case, specifically ROP16), and that paracrine effects
596 are also in play, are similar to the conclusions reached here.

597 Of note, the host response to MIGs + parasites was especially subtle, given that
598 parasite invasion involves dramatic, mechanical perturbations to host cells that might be
599 expected to trigger transcriptional responses. As we did not use host cells containing
600 MIGs and no parasites or vice versa, we could not discern the impact of the MIGs in
601 isolation. Nonetheless, it is tempting to speculate that the response to MIGs + parasites
602 may reflect MIGs counteracting the effects associated with parasite penetration and
603 PVM formation, which may explain the subtle net inflammatory response.
604 In addition, the presence of ROPs and MDGs that respectively activate and
605 suppress certain host processes might be interpreted as energetically wasteful. Why
606 might *Toxoplasma*, an obligate intracellular organism likely under selective pressure for
607 transcriptional efficiency, expend extra resources on effectors that negate one other's
608 effects? One possibility is that ROPs may have undergone selection optimizing for
609 functions required to establish and protect the parasite's intracellular niche (4-9, 47-52),
610 but may also trigger unavoidable host responses detrimental to the parasite. In this
611 scenario, MDGs and paracrine effects could ameliorate such ROP-triggered side effects
612 while theoretically leaving processes beneficial to the parasite intact. Another possibility
613 is that ROPs and GRAs could grant *Toxoplasma* the ability to fine tune host responses
614 in terms of timing and/or magnitude, likely an advantage to an organism that must be
615 equipped to encounter a diversity of intracellular environments due to its extraordinarily
616 broad host range (1, 53, 54).
617 Our analysis also reveals a striking effect on the host cell cycle, in which U-I cells
618 exhibit enrichment of G2/M phase cells. Curiously, this enrichment appeared not to be
619 preserved at 3 hpi, which suggests that the responsible parasite factors exert only a

620 transient influence on host cell cycle-related genes. Of the parasite effectors currently
621 known to modulate the host cell cycle (19, 22, 23, 40, 55), ROP16 is most likely to
622 explain these results: ROP16 phosphorylates ubiquitin-like containing PHD and RING
623 finger domain 1 (UHRF1) in a manner that peaks at 3 hpi, which leads to epigenetic
624 silencing of cyclin B1 (40), a component of the cyclin B1/Cdk1 complex required for the
625 G2/M transition. However, ROP16 is likely not the only ROP to impinge on the host cell
626 cycle, as comparison of G1 phase U-I vs. U-U cells also revealed enrichment in the p53
627 Pathway and KRAS Signaling Up gene sets (Fig. 3; Fig. 8A and Fig. 8B, ROPs), whose
628 corresponding pathways promote cell cycle progression. Further analysis of U-I cells
629 from yet more time points and particularly those not in G1 may shed more light on this
630 interplay.

631 Finally, our analyses thus far reflect a fraction of the possible uses of our dataset,
632 which includes variables of time, parasite strain, infection status, cell cycle phases, and
633 UMAP populations. For example, our dataset includes reads not only from host cells but
634 also the *Toxoplasma* parasites, rendering the data a co-transcriptomic resource that will
635 likely illuminate novel host-parasite interactions. Furthermore, because of limiting
636 numbers, the analyses described here dealt primarily with G1 phase cells in UMAP
637 population 1 and largely excluded cells in the remaining cell cycle phases and UMAP
638 populations. Future analyses of such cells may reveal roles for cell cycle phase, host
639 cell type, or other host-dependent processes.

640

641

642

643 **Materials and Methods**

644 Cell and Parasite Culture

645 All *Toxoplasma gondii* strains were maintained by serial passage in human
646 foreskin fibroblasts (HFFs) cultured at 37ºC in 5% carbon dioxide (CO_2) in complete
647 Dulbeco's Modified Eagle Medium (cDMEM) supplemented with 10% heat-inactivated
648 fetal bovine serum (FBS), 2 mM L-glutamine, 100 U/ml penicillin, and 100 μg/ml
649 streptomycin.

650

651 Construction of Parasite Strains

652 RH Tfn-BLA TdTomato parasites were constructed by transfecting ~10^7 RH
653 Toxofilin-HA-beta-lactamase (RH Tfn-BLA) parasites (8) with the plasmid pSAT1::Cas9-
654 U6::sgUPRT (56) and with the linearized $pCTR_{2T}$ plasmid containing the construct to
655 express TdTomato (57) using the AMAXA Nucleofector 4D system (U-033 setting) and
656 the P3 primary cell 4D-nucleofector X kit with the 16-well nucleocuvette strip (Lonza,
657 V4XP-3032). Clones were obtained by FACS using the FACS Aria II sorter at the
658 Stanford Shared FACS Facility for the brightest red parasites and single cloning the
659 TdTomato+ enriched population by limiting dilution into 96-well plates.

660 A CRISPR-Cas9 strategy was used to construct RH *Δmyr1* mCherry Tfn-BLA
661 parasites from an RH *Δmyr1* mCherry parental strain (25). The parental strain was
662 transfected with the plasmid pSAG1::Cas9-U6::sgUPRT and a linear construct that
663 contained Toxofilin-HA-Beta-lactamase (Tfn-HA-BLA) expressed under *toxofilin*'s
664 endogenous promoter. The Tfn-HA-BLA construct was PCR amplified from the plasmid
665 SP3 (8) such that the final amplicon was flanked by 20 nucleotide (nt) homology arms to

666 the *UPRT* gene that are identical to those used to target constructs to the *UPRT* locus
667 in (56). 15 μg of pSAG1::Cas9-U6::sgUPRT and 3 μg of the Tfn-HA-BLA linear
668 amplicon were transfected into ~10^7 parental strain parasites using the AMAXA
669 Nucleofector 4D system as described above, except the setting on the nucleofector (T-
670 cell human unstimulated HE setting). Selection for parasites with 5 μM 5-
671 fluorodeoxyuridine (FUDR) began at 1 day post-transfection and proceeded for 3 lytic
672 cycles in monolayers of human foreskin fibroblasts (HFFs). The transfected, selected
673 parasite populations were subjected to two rounds of single cloning, one to generate
674 populations of parasites enriched for the presence of the Tfn-HA-BLA construct, and
675 one to purify for individual parasite clones containing the construct, where the readout
676 for the presence of the construct was cleavage of the BLA-cleavable FRET-based dye
677 CCF2-AM, which results in a fluorescence color shift.
678 IFA of monolayers infected with newly constructed RH *Δmyr1* mCherry Tfn-BLA
679 parasites was used to validate correct localization of the Tfn-HA-BLA construct to the
680 parasite rhoptry organelles and the absence of expression of host factors known to be
681 induced in the host nucleus as a result of MYR-dependent GRAs. Coverslips seeded
682 with confluent HFF monolayers were infected with putative RH *Δmyr1* mCherry Tfn-BLA
683 clones for ~24 hours, fixed in 4% formaldehyde for 20 minutes, permeabilized in 0.2%
684 Triton X-100 for 20 minutes, blocked in 1x PBS containing 3% bovine serum albumin (3%
685 BSA solution) for 1 hour at room temperature, stained with primary and secondary
686 antibodies in 3% BSA solution, and mounted onto glass slides using DAPI-containing
687 VectaShield (Vector Laboratories, H-1200) and sealed with colorless nail polish. For
688 Tfn-HA-BLA localization, primary antibodies were mouse-anti-ROP2/3/4 (1:250 dilution,

689 4A7, (58)) and rat anti-HA (1:500, clone 3F10, Sigma Aldrich, 11867431001), and
690 secondary antibodies were goat anti-mouse IgG-Alexa 647 (1:2000 dilution, Thermo
691 Fisher, A-21235) and goat anti-rat IgG-Alexa 488 (1:2000 dilution, Thermo Fisher, A-
692 11006). To verify the absence of the MYR1 protein, the primary antibody rabbit anti-c-
693 myc (1:600 dilution, Sigma, M5546) and the secondary antibody goat anti-rabbit IgG-
694 Alexa 594 (1:2000 dilution, Thermo Fisher, A-11012) were used, and coverslips were
695 seeded with either >3-week-old confluent HFF monolayers or with younger monolayers
696 that had been serum starved for at least 24 hours (using 0.5% FBS instead of 10% FBS
697 in the culture medium) to ensure no spurious induction of c-myc in uninfected host cells.
698 Only clones where the anti-HA and anti-ROP2/3/4 signal colocalized and where no
699 expression of c-myc was detected in the infected host nucleus were selected. RH Tfn-
700 HA-BLA TdTomato parasites (32) and the parental RH *Δmyr1* mCherry parasites were
701 also subjected to both protocols as positive and negative controls, respectively.
702 Coverslips were imaged either on the Stanford Neuroscience Imaging Service core's
703 Zeiss LSM 710 confocal microscope or on an Olympus BX60 upright fluorescence
704 microscope.
705 Western blot was used to verify for the correct size of the Tfn-HA-BLA fusion
706 protein expressed in RH *Δmyr1* mCherry Tfn-BLA parasite clones. Lysates were
707 generated by treatment of parasite pellets with SDS-PAGE loading dye containing 10%
708 beta-mercaptoethanol. The lysates were separated by SDS-PAGE and transferred to a
709 PVDF membrane, and the membrane was blocked with TBST (TBS, 0.05% Tween-20)
710 containing 5% milk for 1.25 hours. The membrane was incubated with horseradish
711 peroxidase (HRP)-conjugated rat anti-HA (clone 3F10) monoclonal antibodies (Roche,

712 Indianapolis, IN) at a dilution of 1:5,000 for 2 hours, and with 1:10,000 dilution rabbit
713 anti-SAG1 for 30 minutes followed by 1:20,000 dilution goat anti-rabbit-HRP for 30
714 minutes, and developed using the ECL Prime Western Blotting System (Sigma-Aldrich,
715 RPN2232).
716
717 Determination of Time to Division for Infected 10 T1/2 Cells
718 To determine the time post-infection at which infected 10 T1/2 cells divided, 10
719 T1/2 host cell monolayers were infected with RH Tfn-BLA TdTomato parasites, and the
720 infected monolayers were imaged by time lapse microscopy.
721 To prepare the parasites for the infection, the parasites were released from
722 heavily infected monolayers of HFFs by mechanical disruption of the monolayers using
723 sterile, disposable scrapers and passage at least 6 times through a 25 gauge syringe.
724 The parasites were washed by pelleting out HFF debris (133.5-208.5 x g for 5 minutes)
725 and resuspending the parasite pellet generated by spinning the remaining supernatant
726 469.2 x g in phenol red-negative low serum DMEM.
727 To prepare the host cell monolayers, 10 T1/2 cells approximately 1 week from
728 their date of thaw were seeded into 12-well tissue culture plates at approximately 6.0 x
729 10^4, 1.2 x 10^5, and 2.4 x 10^5 cells per well. The 10 T1/2 cells were then incubated for >2
730 hours in cDMEM, serum starved by incubation at 37°C in 5% CO_2 in low serum DMEM
731 (i.e., cDMEM containing 0.5% FBS instead of 10% FBS) for 23 hours, washed and
732 stained with 500 μl of Cell Tracker Green CMFDA (CTG-CMFDA; Thermo Fisher,
733 C2925) diluted 1:1000 in prewarmed PBS for 30 minutes at 37°C in 5% CO_2, and
734 washed and incubated in phenol red-negative low serum DMEM (Thermo Fisher,

735 31053028) for 30 minutes. At 24 hours post-infection, RH Tfn-BLA TdTomato parasites
736 were added to the monolayers at a multiplicity of infection (MOI) of 6.
737 Time lapse, epifluorescence images of the infected monolayers were acquired
738 over 16 hours in a controlled (37°C and 5% CO_2) environment using a Nikon Eclipse
739 inverted microscope (Julie Theriot lab). Images were acquired every 20 minutes using
740 100 ms of exposure at 25% power for the Phase, mCherry (to visualize parasites), and
741 GFP (to visualize host cytoplasmic CTG-CMFDA) channels. Cells that were uninfected
742 at the start of the time lapse were followed to determine whether they were infected by
743 the end of the time lapse, as determined by: 1) clearing of cytoplasmic CTG-CMFDA in
744 the exact position of the parasite, 2) disappearance of birefringence in the Phase
745 channel upon parasite invasion, and c) the parasite tracking with the cell at all time
746 points following presumed infection. For each cell for which the precise moment of
747 infection was captured in the live video footage, the time to division was determined
748 using the time the cell was infected as the start time and the time the cell divided (if
749 applicable) as the end time.
750
751 <u>FACS of Single Uninfected-Injected (U-I) Cells for Single Cell RNA Sequencing</u>
752 <u>(scRNA-seq)</u>
753 *Preparation of Single Cells for FACS Sorting*
754 To generate U-I cells for FACS sorting, 10 T1/2 host cells approximately 1 week
755 from their date of thaw were seeded into 6-well tissue culture plates at a density of
756 approximately 2.6 x 10^5 cells per well, incubated for >2 hours in cDMEM, and serum
757 starved by incubation in low serum DMEM (i.e., cDMEM containing 0.5% FBS instead of

758 10% FBS) for 24 hours. 10 T1/2 host cells were chosen as they are monolayer-forming,
759 contact-inhibited fibroblasts that are also suitable for single cell sorting due to adequate
760 dissociation into individual cells by a combination of mechanical and chemical disruption.
761 Next, either RH Tfn-BLA or RH *Δmyr1* mCherry Tfn-BLA parasites were released from
762 heavily infected monolayers of HFFs by mechanical disruption of the monolayers using
763 sterile, disposable scrapers and passage at least 6 times through a 25 gauge syringe.
764 Parasite-free lysate was similarly generated by mechanical disruption of uninfected
765 HFFs. Parasites and parasite-free lysate were washed by pelleting out HFF debris
766 (133.5-208.5 x g for 5 minutes) and resuspending the parasite pellet generated by
767 spinning the remaining supernatant 469.2 x g in low serum DMEM containing either 1
768 μM DMSO (for the wild type and *Δmyr1* conditions) or with 1 μM of the invasion inhibitor
769 cytochalasin D (cytD, for the cytD-treated wild type condition), incubated at room
770 temperature for 10 minutes, and applied to the serum starved 10 T1/2 monolayers at
771 MOI = 6, which maximized the abundance of U-I cells in tissue culture. All 10 T1/2
772 monolayers were spun at 469.2 x g for 5 minutes to synchronize parasite contact with
773 the monolayer. Infections were allowed to proceed for 30 minutes, 1.5 hours, or 2.5
774 hours at 37°C. Because cytD is a reversible inhibitor, extra cytD-containing low serum
775 DMEM was added to each of the drug-treated infections to maintain the concentration of
776 cytD at 0.5-1 μM for the entire infection duration.
777 To identify host cells injected by parasite proteins, a 6x stock solution of the BLA
778 substrate CCF2-AM (Thermo Fisher, K1032) was added to the media over 10 T1/2 cells
779 so that the final concentration of CCF2-AM was 1x. CCF2-AM treated monolayers were
780 incubated under foil (to protect from light) for 30 minutes at room temperature (to

781 prevent breakdown of CCF2-AM, which degrades at 37°C), bringing up the total
782 infection duration to 1 h, 2 h, and 3 h.
783 To harvest the 10 T1/2 monolayers for subsequent FACS analysis, the
784 monolayers were: 1) washed 3 times in 1x phosphate buffered saline (PBS) to remove
785 any HFF debris adhering to the monolayer; 2) incubated in trypsin (prepared in plastic
786 vessels only) at room temperature for 6-10 minutes; 3) quenched in an equal volume of
787 FACS buffer (1 x PBS + 2% FBS + 50 mM $MgCl_2$*$6H_20$ + 50 μg/ml DNase I); 4) passed
788 3 times through an 18 gauge syringe to break any residual cell clumps; and 5) washed
789 in FACS buffer to remove excess trypsin. Of note, DNase I and $MgCl_2$ were included in
790 the FACS buffer to prevent clumping of cells from cell death. The cells were then
791 stained with a viability dye and an extracellular parasite stain by 1) resuspending them
792 in 500 μl of chilled 4°C 1x PBS containing 3% bovine serum albumin (BSA) and 1:500
793 dilution rabbit anti-SAG2A primary antibody (gift of C. Lekutis) for 30 minutes on wet ice,
794 2) washing them in 5 ml of ice cold 1x PBS and spinning at 133.5 x g (lowest setting) at
795 4°C for 5 minutes, and 3) resuspending the pellets in chilled 1x PBS containing 3% BSA,
796 1:1000 dilution goat anti-rabbit IgG-Alexa 647 (Thermo Fisher), and 3 μl/ml near-
797 infrared live/dead fixable viability dye (Thermo Fisher, L94375) for 30 minutes on wet
798 ice. Samples were then washed as before, the pellets were resuspended in 1 ml of
799 chilled FACS buffer, and the cell suspension was transferred through a nylon filter cap
800 (Thomas Scientific, 4620F40) into polypropylene FACS tubes stored on wet ice and
801 protected from light until FACS sorting.
802
803 *FACS of Single Cells*

804 To prepare the multi-well lysis plates into which cells were deposited during
805 FACS sorting, lysis buffer was dispensed either by the Mantis liquid handling robot
806 (Formulatrix) at 0.4 μl per well into 384-well hard shell low profile PCR plates (Bio-rad)
807 for single cell RNA sequencing, or by hand at 5 μl per well into 96-well hard shell low
808 profile PCR plates (Bio-rad) for bulk RNA sequencing. Lysis buffer was prepared in
809 batches of 8 ml by mixing 5.888 ml water, 160 μl recombinant RNase inhibitor (Takara
810 Clonetech), 1.6 ml of 10 mM dNTP (Thermo Fisher), 160 μl of 100 μM oligo-dT (iDT),
811 1:600,000 diluted ERCC spike-in RNA molecules (Thermo Fisher), and 32 μl 10% Triton
812 X-100. All reagents were declared RNase free. Lysis plates were prepared the night
813 before each FACS sort, stored overnight at -80°C, and kept on dry ice during the FACS
814 sort.
815 All host cell samples were sorted at the Stanford Shared FACS Facility (SSFF)
816 by the BD Influx Special Order sorter using the following channels: forward scatter (488
817 nm blue laser, SSC detector), side scatter (488 nm blue laser, FSC detector), BV421
818 (405 nm violet laser, V460 detector, which detected cleaved CCF2-AM), BV510 (405
819 nm violet laser, V520 detector, which detected uncleaved CCF2-AM), mCherry (561 nm
820 yellow laser, Y610 detector, which detected parasite-associated cells), APC (640 nm
821 red laser, R670 detector, which detected the extracellular parasite stain vs. anti-SAG2A),
822 and APC-Cy7 (640 nm red laser, R750 detector, which detected dead cells). Gating
823 strategy used to obtain U-I cells is indicated in Fig. 1D. More specifically, cells without
824 red fluorescence (i.e., parasite-free) but with enhanced signal from cleaved CCF2-AM
825 (i.e., injected) were sorted as U-I cells, while those with red fluorescence (i.e., parasite-
826 associated), enhanced signal from CCF2-AM (i.e., injected), and low extracellular

827 parasite stain were sorted as I-I cells. Of note, the parasite-associated gate, from which
828 I-I cells were obtained, was intentionally kept narrow to ensure host cells were each
829 infected with approximately one parasite apiece, which limited confounding downstream
830 analysis with penetration of >1 parasite at two different time points. Single color and
831 colorless controls were used for compensation and adjustment of channel voltages.
832 Fluorescence data were collected with FACSDiva software and analyzed with Flowjo
833 software. Cells were index sorted such that each cell's fluorescence data were recorded
834 for subsequent analysis. For single cell experiments, cells were sorted into the 384-well
835 lysis plates at 1 cell per well. For bulk experiments, cells were sorted into 96-well lysis
836 plates at 50-100 cells per well. Plates were sealed with foil plate sealers and
837 immediately placed on dry ice until the completion of the sort. Plates were then stored at
838 -80°C until library preparation.
839
840 cDNA Synthesis from Single Cell RNA, Library Preparation, and Sequencing
841 To convert the RNA obtained from single cells and bulk samples to cDNA, we
842 employed the Smart-seq2 protocol (59). For single cell library preparation, the liquid
843 handling robots Mantis (Formulatrix) and Mosquito (TTP Labtech) were employed to
844 transfer and dispense small volumes of reagents, and final reaction volume was 2 μl per
845 well. For bulk sample library preparation, liquid handling was performed with standard
846 multichannel pipets and final reaction volume was 25 μl per sample. cDNA was subject
847 to 19 round of pre-amplification and then quantified using EvaGreen and diluted in EB
848 buffer to obtain a final concentration of 0.4-0.8 ng/μl per sample. Library preparation
849 continued using in-house Tn5 tagmentation. For single cell libraries, we used custom

850 barcoded indices for each cell, and for bulk libraries, we used Nextera XT indices.
851 Libraries were submitted to the Chan Zuckerberg Biohub Genomics Core for
852 sequencing. Single cell libraries were sequenced on the NovaSeq 6000 by 2x150 base
853 pair paired end sequencing aiming at ~1 million reads per cell. Bulk libraries were
854 sequenced on the NextSeq by 2x150 base pair paired end sequencing at ~10 million
855 reads per sample.
856 For library preparation, the liquid handling robots Mantis and Mosquito were
857 employed to transfer and dispense small volumes of reagents, and final reaction volume
858 was 2 μl per cell. For bulk sample library preparation, liquid handling was performed
859 with standard multichannel pipets and final reaction volume was 25 μl per sample.
860 cDNA was subject to 19 round of pre-amplification and then quantified using EvaGreen
861 and diluted in EB buffer to obtain a final concentration of 0.4-0.8 ng/μl per sample.
862 Library preparation continued using in-house Tn5 tagmentation. For single cell libraries,
863 we used custom barcoded indices for each cell, and for bulk libraries, we used Nextera
864 XT indices. Libraries were submitted to the Chan Zuckerberg Biohub Genomics Core for
865 sequencing. Single cell libraries were sequenced on the NovaSeq 6000 by 2x150 base
866 pair paired end sequencing aiming at ~1 million reads per cell. Bulk libraries were
867 sequenced on the NextSeq by 2x150 base pair paired end sequencing at ~10 million
868 reads per sample.
869
870 Sequencing Alignment
871 Reads output from sequencing were aligned to a concatenated genome
872 composed of the mouse genome (GRCm build 38) and the GT1 *Toxoplasma gondii*

873 genome (ToxoDB version 36), which is the most complete reference for type I parasite
874 strains such as the RH strains used in this work. Alignment was performed using STAR,
875 and transcript counting was performed by Htseq-count, with standard parameters used
876 for both packages. A custom python script was used to sum transcript counts to yield a
877 final gene count matrix consisting of all sequenced cells and the number of read counts
878 detected for each gene.
879
880 Data Preprocessing
881 To filter out cells of poor quality from the analysis, we excluded cells based on
882 the following metrics: gene count, total read sum, percentage of reads that mapped to
883 the mouse-*Toxoplasma* concatenated genome, percentage of reads derived from
884 spiked in ERCC standards, and percentage of reads derived from ribosomal RNA.
885 The gene count matrices were then normalized as counts per median (cpm).
886 Briefly, we first calculated the sum of reads for all cells. We then divided the read counts
887 by the corresponding sum of reads in each cell and multiplied the fractional count by the
888 median of the sum of reads as a scaling factor. Normalized data were transformed to
889 log2 space after adding a pseudo-count of 1 for each gene of each cell.
890 To determine the detection limit of each experimental trial (e.g., the 50%
891 detection rate), we computed a logistic regression model from a plot of the detection
892 probability for spiked-in ERCC standards. We then excluded genes where less than 5
893 cells in the experimental trial expressed that gene at a level above the detection limit.
894 To identify host genes associated with infection, we first excluded mouse genes
895 to which *Toxoplasma* sequences erroneously map by aligning RNA sequences obtained

896 from single cell extracellular RH parasites to the concatenated mouse-*Toxoplasma*
897 genome and eliminating all mouse genes with an average $\log_2$(cpm+1) expression of
898 0.2 or greater.
899
900 Single Cell vs. Bulk Sample Correlation Analysis
901 To validate the single cell expression data, we plotted the log2 mean expression
902 of each differentially expressed gene, as identified by the MAST algorithm using the
903 single cell data, in single cells vs. bulk samples. The sklearn package was applied to
904 compute linear regression and the corresponding R^2 values.
905
906 Cell Cycle Analysis and Annotation
907 To predict the cell cycle phase of individual single cells, we curated a list of 175
908 cell cycle marker genes from the literature (60-67) and from the database CycleBase
909 3.0 (68). We computed the first two principle components of the gene count matrix using
910 principle component analysis (PCA) and projected the cells. We partitioned the cells
911 using K-Means clustering and assigned the clusters with their predicted cell cycle
912 phases (G1, S, and G2/M) based on the expression of 175 cell cycle marker genes
913 curated from the literature (Table S2).
914
915 Dimensionality Reduction
916 To visually represent relationships between single cells across all experimental
917 trials based on their transcriptional variation regardless of experimental conditions, we
918 identified and filtered for the top 1000 genes with the highest dispersion (i.e., the genes

919 with the most variable expression for their bin groups with similar expression level)
920 across all datasets, applied mutual nearest neighborhood batch correction (MNNPY) to
921 correct for batch effects, and projected the data onto two dimensional space with the
922 uniform manifold approximation and projection (UMAP) algorithm using default
923 parameters in Scanpy (69). Leiden clustering using the top 1000 dispsered genes
924 enabled partitioning of cells into three populations (1, 2, and 3), which we separated into
925 individual datasets for downstream analysis.
926
927 Infection Status Classification
928 We also determined the host infection load by quantifying the percent of reads
929 that mapped to *Toxoplasma* in a given sample. We filtered samples which were shown
930 by FACS to exhibit one presumed infection status (based on red fluorescence from
931 internalized parasites) but were determined to exhibit the opposite or an ambiguous
932 infection status otherwise (based on percentage of reads derived from *Toxoplasma*).
933
934 Differential Expression Analysis
935 To obtain differentially expressed genes (DEGs) between all pairs of conditions,
936 we used the Model-based Analysis of Single Cell Transcriptomics (MAST) algorithm (70)
937 to compute the results on all G1, correctly classified, and UMAP population 1 cells. We
938 used the default settings except with an adaptive conditional mean of expression based
939 on 20 number of bins, at least 30 genes in each bin, and we did not filter out any gene
940 with non-zero expression frequency in the samples.
941

942 Gene Set Enrichment Analysis

943 We performed gene set enrichment analysis (GSEA) on the lists of differentially
944 expressed genes between all pairs of experimental conditions, ranked by their relative
945 expression in each of the two conditions, for each individual experimental trial using the
946 fast pre-ranked gene set enrichment analysis (fgsea) package (71). Genes were
947 compared to the Molecular Signature Database's Hallmarks gene sets. Pathways with
948 an adjusted p-value (FDR) of < 0.25 were considered to be significantly enriched at the
949 top or the bottom of the ranked list of differentially expressed genes.

950

951 Identification of Differentially Regulated Genes between Conditions Using CCF2-AM
952 Ratio Correlation Analysis

953 To identify host genes associated with injection, we first computed the CCF2-
954 ratio for each cell, a metric that serves as a readout for parasite effector injection and
955 that was calculated by dividing the log-transformed cleaved CCF2-AM fluorescence by
956 the log-transformed uncleaved CCF2-AM fluorescence. Next, we excluded mouse
957 genes below the detection limit and mouse genes to which *Toxoplasma* sequences
958 erroneously map. Finally, for each infected or injected condition (i.e., Wt U-I, Wt I-I,
959 Dmyr1 U-I, Dmyr1 I-I, CytD U-I, and CytD I-I), we computed the Spearman correlation of
960 each of the remaining genes to the CCF2-AM ratio using cells from the condition of
961 interest and cells from the cognate U-U condition (e.g., to calculate Spearman
962 correlations for Wt U-I cells, we correlated gene expression to the CCF2-AM ratio in Wt
963 U-I and Wt U-U cells).

964 To identify genes differentially regulated between pairs of conditions using the
965 CCF2-AM correlation data, we generated scatterplots where each data point
966 represented a gene and its displacement on each of the x- and y-axes represented the
967 Spearman correlation in each of the conditions. We modeled a Gaussian distribution
968 using the Sklearn package with default parameters with settings "n_components=1" and
969 "covariance_type='full'". Genes with a difference in CCF2-AM correlation score of >0.2
970 or <-0.2 and whose probability densities were more than three standard deviations from
971 the mean probability density were considered to exhibit significant differential
972 expression between the pair of conditions under scrutiny.
973
974 Generation of Strip Plots
975 Strip plots in Fig. 7B were generated using seaborn's catplot and boxplot
976 packages to plot the normalized expression scores for each cell across 11 experimental
977 conditions for differentially expressed genes (DEGs) between Dmyr1 U-U and Mock
978 samples. The normalized expression score for each cell was calculated by 1)
979 subtracting the minimum log2 cpm for that gene across all cells in the experiment, 2)
980 dividing the difference by the maximum log2 cpm across all cells, such that the cell with
981 the lowest count receives a score of 0 and the cell with the highest count receives a
982 score of 1, and 3) computing the average of the normalized cpm's for each cell.
983
984 Generation of Bubble Plots
985 Bubble plots in Fig. 8A and Fig. 8B were generated using a custom Python script
986 in which columns indicated the gene set and rows indicated the comparison (taken to

987 signify the impact of one to a few parasite-dependent stimuli on host transcription) from
988 which the gene sets were enriched. The bubbles in each plot were color coded and
989 sized based on one of two schemes. In the first scheme, bubble color indicated the
990 normalized enrichment score, where scores were positive if the genes corresponding to
991 a given gene set were expressed higher in the first member of the pair in the given
992 comparison than in the second member of the pair, and bubble size indicated the
993 significance (FDR) of the enrichment, where the absolute size of each bubble
994 corresponded to the reciprocal of the FDR. In the second scheme, bubble color
995 indicated the log2 normalized fold change in expression of DEGs from a given
996 comparison that also corresponded to a given Hallmark pathway, where positive fold
997 changes indicated genes were expressed higher in the first member of the pair in the
998 comparison than in the second member, and bubble size indicated the number of DEGs
999 used to calculate the fold change. To calculate fold change for each given comparison's
1000 gene set, DEGs from the comparison that fell under the gene set were identified,
1001 expression of these DEGs in cpm was normalized across all cells to a maximum value
1002 of 1 and averaged across all the cells in each condition, and average normalized
1003 expression in the first experimental condition was divided by average normalized
1004 expression in the second experimental condition.
1005

1006 **Acknowledgments**

1007 Special thanks to Terence Theisen for his assistance in preparing U-I cells for
1008 FACS sorting; Meredith Weglarz and Marty Bigos from the Stanford Shared FACS
1009 Facility for their assistance during the FACS sorts for U-I cells; and David Parks and

1010 Catherine Carswell-Crumpton for their input in optimizing the FACS sort conditions to
1011 obtain pure U-I cell populations. We also thank Saroja Kolluru and Robert Jones for
1012 their assistance during library preparation and sample submission, Fabio Zanini for
1013 experimental suggestions, Geoff Stanley and Michelle Chen for their input on the
1014 bioinformatic analysis of the U-I scRNAseq data, and Julie Theriot, Zhou Xiaoxue, and
1015 Matthew J. Footer for their assistance with the live video microscopy experiments. This
1016 work was supported by NIH F30 AI124589-03 (SR), Stanford Interdisciplinary Graduate
1017 Bio-X Fellowship (YX), RO1 AI021423 and AI129529 (JCB), Chan Zuckerberg Biohub
1018 (SRQ), NIH S10 Shared Instrument Grant S110RR025518-01 (Stanford Shared FACS
1019 Facility), and NIH NS069375 (Neuroscience Microscopy Core).
1020
1021
1022
1023
1024
1025
1026
1027
1028
1029
1030
1031
1032

1033 **REFERENCES**

1034 1. J. P. Dubey CPB. 1988. Toxoplasmosis of Animals and Man. CRC Press, Boca Raton.

1035 2. Blader IJ, Coleman BI, Chen CT, Gubbels MJ. 2015. Lytic Cycle of Toxoplasma gondii: 15
1036 Years Later. Annu Rev Microbiol 69:463-85.

1037 3. Rastogi S, Cygan AM, Boothroyd JC. 2019. Translocation of effector proteins into host
1038 cells by Toxoplasma gondii. Curr Opin Microbiol 52:130-138.

1039 4. Fleckenstein MC, Reese ML, Konen-Waisman S, Boothroyd JC, Howard JC, Steinfeldt T.
1040 2012. A Toxoplasma gondii pseudokinase inhibits host IRG resistance proteins. PLoS Biol
1041 10:e1001358.

1042 5. Reese ML, Shah N, Boothroyd JC. 2014. The Toxoplasma Pseudokinase ROP5 Is an
1043 Allosteric Inhibitor of the Immunity-related GTPases. J Biol Chem 289:27849-58.

1044 6. Etheridge RD, Alaganan A, Tang K, Lou HJ, Turk BE, Sibley LD. 2014. The Toxoplasma
1045 pseudokinase ROP5 forms complexes with ROP18 and ROP17 kinases that synergize to
1046 control acute virulence in mice. Cell Host Microbe 15:537-50.

1047 7. Li JX, He JJ, Elsheikha HM, Chen D, Zhai BT, Zhu XQ, Yan HK. 2019. Toxoplasma gondii
1048 ROP17 inhibits the innate immune response of HEK293T cells to promote its survival.
1049 Parasitol Res 118:783-792.

1050 8. Lodoen MB, Gerke C, Boothroyd JC. 2010. A highly sensitive FRET-based approach
1051 reveals secretion of the actin-binding protein toxofilin during Toxoplasma gondii
1052 infection. Cell Microbiol 12:55-66.

1053 9. Delorme-Walker V, Abrivard M, Lagal V, Anderson K, Perazzi A, Gonzalez V, Page C,
1054 Chauvet J, Ochoa W, Volkmann N, Hanein D, Tardieux I. 2012. Toxofilin upregulates the

1055 host cortical actin cytoskeleton dynamics, facilitating Toxoplasma invasion. J Cell Sci
1056 125:4333-42.
1057 10. Ong YC, Reese ML, Boothroyd JC. 2010. Toxoplasma rhoptry protein 16 (ROP16)
1058 subverts host function by direct tyrosine phosphorylation of STAT6. J Biol Chem
1059 285:28731-40.
1060 11. Yamamoto M, Standley DM, Takashima S, Saiga H, Okuyama M, Kayama H, Kubo E, Ito H,
1061 Takaura M, Matsuda T, Soldati-Favre D, Takeda K. 2009. A single polymorphic amino
1062 acid on Toxoplasma gondii kinase ROP16 determines the direct and strain-specific
1063 activation of Stat3. J Exp Med 206:2747-60.
1064 12. Saeij JP, Coller S, Boyle JP, Jerome ME, White MW, Boothroyd JC. 2007. Toxoplasma co-
1065 opts host gene expression by injection of a polymorphic kinase homologue. Nature
1066 445:324-7.
1067 13. Mercier C, Dubremetz JF, Rauscher B, Lecordier L, Sibley LD, Cesbron-Delauw MF. 2002.
1068 Biogenesis of nanotubular network in Toxoplasma parasitophorous vacuole induced by
1069 parasite proteins. Mol Biol Cell 13:2397-409.
1070 14. Sibley LD, Niesman IR, Parmley SF, Cesbron-Delauw MF. 1995. Regulated secretion of
1071 multi-lamellar vesicles leads to formation of a tubulovesicular network in host-cell
1072 vacuoles occupied by *Toxoplasma gondii*. J Cell Sci 108:1669-1677.
1073 15. Gold DA, Kaplan AD, Lis A, Bett GC, Rosowski EE, Cirelli KM, Bougdour A, Sidik SM, Beck
1074 JR, Lourido S, Egea PF, Bradley PJ, Hakimi MA, Rasmusson RL, Saeij JP. 2015. The
1075 Toxoplasma Dense Granule Proteins GRA17 and GRA23 Mediate the Movement of Small

1076 Molecules between the Host and the Parasitophorous Vacuole. Cell Host Microbe
1077 17:642-52.
1078 16. Pernas L, Adomako-Ankomah Y, Shastri AJ, Ewald SE, Treeck M, Boyle JP, Boothroyd JC.
1079 2014. Toxoplasma effector MAF1 mediates recruitment of host mitochondria and
1080 impacts the host response. PLoS Biol 12:e1001845.
1081 17. Cesbron-Delauw MF, Guy B, Torpier G, Pierce RJ, Lenzen G, Cesbron JY, Charif H, Lepage
1082 P, Darcy F, Lecocq JP, et al. 1989. Molecular characterization of a 23-kilodalton major
1083 antigen secreted by Toxoplasma gondii. Proc Natl Acad Sci U S A 86:7537-41.
1084 18. Gay G, Braun L, Brenier-Pinchart MP, Vollaire J, Josserand V, Bertini RL, Varesano A,
1085 Touquet B, De Bock PJ, Coute Y, Tardieux I, Bougdour A, Hakimi MA. 2016. Toxoplasma
1086 gondii TgIST co-opts host chromatin repressors dampening STAT1-dependent gene
1087 regulation and IFN-gamma-mediated host defenses. J Exp Med 213:1779-98.
1088 19. Bougdour A, Durandau E, Brenier-Pinchart MP, Ortet P, Barakat M, Kieffer S, Curt-
1089 Varesano A, Curt-Bertini RL, Bastien O, Coute Y, Pelloux H, Hakimi MA. 2013. Host cell
1090 subversion by Toxoplasma GRA16, an exported dense granule protein that targets the
1091 host cell nucleus and alters gene expression. Cell Host Microbe 13:489-500.
1092 20. He H, Brenier-Pinchart MP, Braun L, Kraut A, Touquet B, Coute Y, Tardieux I, Hakimi MA,
1093 Bougdour A. 2018. Characterization of a Toxoplasma effector uncovers an alternative
1094 GSK3/beta-catenin-regulatory pathway of inflammation. Elife 7.
1095 21. Braun L, Brenier-Pinchart MP, Yogavel M, Curt-Varesano A, Curt-Bertini RL, Hussain T,
1096 Kieffer-Jaquinod S, Coute Y, Pelloux H, Tardieux I, Sharma A, Belrhali H, Bougdour A,
1097 Hakimi MA. 2013. A Toxoplasma dense granule protein, GRA24, modulates the early

1098 immune response to infection by promoting a direct and sustained host p38 MAPK
1099 activation. J Exp Med 210:2071-86.
1100 22. Braun L, Brenier-Pinchart MP, Hammoudi PM, Cannella D, Kieffer-Jaquinod S, Vollaire J,
1101 Josserand V, Touquet B, Coute Y, Tardieux I, Bougdour A, Hakimi MA. 2019. The
1102 Toxoplasma effector TEEGR promotes parasite persistence by modulating NF-kappaB
1103 signalling via EZH2. Nat Microbiol doi:10.1038/s41564-019-0431-8.
1104 23. Panas MW, Naor A, Cygan AM, Boothroyd JC. 2019. Toxoplasma Controls Host Cyclin E
1105 Expression through the Use of a Novel MYR1-Dependent Effector Protein, HCE1. MBio
1106 10.
1107 24. Nadipuram SM, Kim EW, Vashisht AA, Lin AH, Bell HN, Coppens I, Wohlschlegel JA,
1108 Bradley PJ. 2016. In Vivo Biotinylation of the Toxoplasma Parasitophorous Vacuole
1109 Reveals Novel Dense Granule Proteins Important for Parasite Growth and Pathogenesis.
1110 MBio 7.
1111 25. Franco M, Panas MW, Marino ND, Lee MC, Buchholz KR, Kelly FD, Bednarski JJ, Sleckman
1112 BP, Pourmand N, Boothroyd JC. 2016. A Novel Secreted Protein, MYR1, Is Central to
1113 Toxoplasma's Manipulation of Host Cells. MBio 7.
1114 26. Marino ND, Panas MW, Franco M, Theisen TC, Naor A, Rastogi S, Buchholz KR, Lorenzi
1115 HA, Boothroyd JC. 2018. Identification of a novel protein complex essential for effector
1116 translocation across the parasitophorous vacuole membrane of Toxoplasma gondii. PLoS
1117 Pathog 14:e1006828.
1118 27. Cygan AM, Theisen, T. C., Mendoza, A. G., Marino, N. D., Panas, M. W., and Boothroyd, J.
1119 C. 2019. Co-immunoprecipitation with MYR1 identifies three additional proteins within

1120 the Toxoplasma parasitophorous vacuole required for translocation of dense granule
1121 effectors into host cells. bioRxiv 867788.
1122 28. Hakimi MA, Olias P, Sibley LD. 2017. Toxoplasma Effectors Targeting Host Signaling and
1123 Transcription. Clin Microbiol Rev 30:615-645.
1124 29. Hirai K, Hirato K, Yanagwa R. 1966. A cinematographic study of the penetration of
1125 cultured cells by Toxoplasma gondii. Jpn J Vet Res 14:81-90.
1126 30. Kimata I, Tanabe K. 1987. Secretion by Toxoplasma gondii of an antigen that appears to
1127 become associated with the parasitophorous vacuole membrane upon invasion of the
1128 host cell. J Cell Sci 88:231-9.
1129 31. Naor A, Panas MW, Marino N, Coffey MJ, Tonkin CJ, Boothroyd JC. 2018. MYR1-
1130 Dependent Effectors Are the Major Drivers of a Host Cell's Early Response to
1131 Toxoplasma, Including Counteracting MYR1-Independent Effects. MBio 9.
1132 32. Koshy AA, Dietrich HK, Christian DA, Melehani JH, Shastri AJ, Hunter CA, Boothroyd JC.
1133 2012. Toxoplasma co-opts host cells it does not invade. PLoS Pathog 8:e1002825.
1134 33. Luder CG, Walter W, Beuerle B, Maeurer MJ, Gross U. 2001. Toxoplasma gondii down-
1135 regulates MHC class II gene expression and antigen presentation by murine
1136 macrophages via interference with nuclear translocation of STAT1alpha. Eur J Immunol
1137 31:1475-84.
1138 34. Kim SK, Fouts AE, Boothroyd JC. 2007. Toxoplasma gondii Dysregulates IFN-{gamma}-
1139 Inducible Gene Expression in Human Fibroblasts: Insights from a Genome-Wide
1140 Transcriptional Profiling. J Immunol 178:5154-65.

1141 35. Dubey JP. 1992. Isolation of Toxoplasma gondii from a naturally infected beef cow. J
1142 Parasitol 78:151-3.
1143 36. Khan A, Behnke MS, Dunay IR, White MW, Sibley LD. 2009. Phenotypic and gene
1144 expression changes among clonal type I strains of Toxoplasma gondii. Eukaryot Cell
1145 8:1828-36.
1146 37. Ziegenhain C, Vieth B, Parekh S, Reinius B, Guillaumet-Adkins A, Smets M, Leonhardt H,
1147 Heyn H, Hellmann I, Enard W. 2017. Comparative Analysis of Single-Cell RNA Sequencing
1148 Methods. Mol Cell 65:631-643 e4.
1149 38. Brunet J, Pfaff AW, Abidi A, Unoki M, Nakamura Y, Guinard M, Klein JP, Candolfi E,
1150 Mousli M. 2008. Toxoplasma gondii exploits UHRF1 and induces host cell cycle arrest at
1151 G2 to enable its proliferation. Cell Microbiol 10:908-20.
1152 39. Molestina RE, El-Guendy N, Sinai AP. 2008. Infection with Toxoplasma gondii results in
1153 dysregulation of the host cell cycle. Cell Microbiol 10:1153-65.
1154 40. Sabou M, Doderer-Lang C, Leyer C, Konjic A, Kubina S, Lennon S, Rohr O, Viville S,
1155 Cianferani S, Candolfi E, Pfaff AW, Brunet J. 2019. Toxoplasma gondii ROP16 kinase
1156 silences the cyclin B1 gene promoter by hijacking host cell UHRF1-dependent epigenetic
1157 pathways. Cell Mol Life Sci doi:10.1007/s00018-019-03267-2.
1158 41. Velasquez ZD, Conejeros I, Larrazabal C, Kerner K, Hermosilla C, Taubert A. 2019.
1159 Toxoplasma gondii-induced host cellular cell cycle dysregulation is linked to
1160 chromosome missegregation and cytokinesis failure in primary endothelial host cells. Sci
1161 Rep 9:12496.

1162 42. Pinney DF, Emerson CP, Jr. 1989. 10T1/2 cells: an in vitro model for molecular genetic
1163 analysis of mesodermal determination and differentiation. Environ Health Perspect
1164 80:221-7.
1165 43. Subramanian A, Tamayo P, Mootha VK, Mukherjee S, Ebert BL, Gillette MA, Paulovich A,
1166 Pomeroy SL, Golub TR, Lander ES, Mesirov JP. 2005. Gene set enrichment analysis: a
1167 knowledge-based approach for interpreting genome-wide expression profiles. Proc Natl
1168 Acad Sci U S A 102:15545-50.
1169 44. Chen L, Christian DA, Kochanowsky JA, Phan AT, Clark JT, Wang S, Berry C, Oh J, Chen X,
1170 Roos DS, Beiting DP, Koshy AA, Hunter CA. 2020. The Toxoplasma gondii virulence factor
1171 ROP16 acts in cis and trans, and suppresses T cell responses. J Exp Med 217.
1172 45. Park E, Patel S, Wang Q, Andhey P, Zaitsev K, Porter S, Hershey M, Bern M, Plougastel-
1173 Douglas B, Collins P, Colonna M, Murphy KM, Oltz E, Artyomov M, Sibley LD, Yokoyama
1174 WM. 2019. Toxoplasma gondii infection drives conversion of NK cells into ILC1-like cells.
1175 Elife 8.
1176 46. Young J, Dominicus C, Wagener J, Butterworth S, Ye X, Kelly G, Ordan M, Saunders B,
1177 Instrell R, Howell M, Stewart A, Treeck M. 2019. A CRISPR platform for targeted in vivo
1178 screens identifies Toxoplasma gondii virulence factors in mice. Nat Commun 10:3963.
1179 47. Poupel O, Boleti H, Axisa S, Couture-Tosi E, Tardieux I. 2000. Toxofilin, a novel actin-
1180 binding protein from Toxoplasma gondii, sequesters actin monomers and caps actin
1181 filaments. Mol Biol Cell 11:355-68.
1182 48. Sinai AP, Joiner KA. 2001. The Toxoplasma gondii protein ROP2 mediates host organelle
1183 association with the parasitophorous vacuole membrane. J Cell Biol 154:95-108.

1184 49. Reese ML, Boothroyd JC. 2009. A helical membrane-binding domain targets the
1185 Toxoplasma ROP2 family to the parasitophorous vacuole. Traffic 10:1458-70.
1186 50. Carey KL, Jongco AM, Kim K, Ward GE. 2004. The Toxoplasma gondii rhoptry protein
1187 ROP4 is secreted into the parasitophorous vacuole and becomes phosphorylated in
1188 infected cells. Eukaryot Cell 3:1320-30.
1189 51. Hajj HE, Lebrun M, Fourmaux MN, Vial H, Dubremetz JF. 2006. Characterization,
1190 biosynthesis and fate of ROP7, a ROP2 related rhoptry protein of Toxoplasma gondii.
1191 Mol Biochem Parasitol 146:98-100.
1192 52. Wei F, Wang W, Liu Q. 2013. Protein kinases of Toxoplasma gondii: functions and drug
1193 targets. Parasitol Res 112:2121-9.
1194 53. Werk R. 1985. How does Toxoplasma gondii enter host cells? Rev Infect Dis 7:449-57.
1195 54. Dubey JP. 2010. Toxoplasma gondii infections in chickens (Gallus domesticus):
1196 prevalence, clinical disease, diagnosis and public health significance. Zoonoses Public
1197 Health 57:60-73.
1198 55. Kim SG, Seo SH, Shin JH, Yang JP, Lee SH, Shin EH. 2019. Increase in the nuclear
1199 localization of PTEN by the Toxoplasma GRA16 protein and subsequent induction of
1200 p53-dependent apoptosis and anticancer effect. J Cell Mol Med
1201 doi:10.1111/jcmm.14207.
1202 56. Shen B, Brown KM, Lee TD, Sibley LD. 2014. Efficient gene disruption in diverse strains of
1203 Toxoplasma gondii using CRISPR/CAS9. MBio 5:e01114-14.
1204 57. van Dooren GG, Tomova C, Agrawal S, Humbel BM, Striepen B. 2008. Toxoplasma gondii
1205 Tic20 is essential for apicoplast protein import. Proc Natl Acad Sci U S A 105:13574-9.

1206 58. Sadak A, Taghy Z, Fortier B, Dubremetz JF. 1988. Characterization of a family of rhoptry
1207 proteins of Toxoplasma gondii. Mol Biochem Parasitol 29:203-11.
1208 59. Picelli S, Faridani OR, Bjorklund AK, Winberg G, Sagasser S, Sandberg R. 2014. Full-length
1209 RNA-seq from single cells using Smart-seq2. Nat Protoc 9:171-81.
1210 60. Zehua Liu HL, Kaikun Xie, Hao Wang, Ning Chen, Oscar M. Aparicio, Machael Q. Zhang,
1211 Rui Jiang, Ting Chen. 2017. Reconstructing cell cycle pseudo time-series via single-cell
1212 transcriptome data. Nature Communications 8:9.
1213 61. Tirosh I, Izar B, Prakadan SM, Wadsworth MH, 2nd, Treacy D, Trombetta JJ, Rotem A,
1214 Rodman C, Lian C, Murphy G, Fallahi-Sichani M, Dutton-Regester K, Lin JR, Cohen O,
1215 Shah P, Lu D, Genshaft AS, Hughes TK, Ziegler CG, Kazer SW, Gaillard A, Kolb KE, Villani
1216 AC, Johannessen CM, Andreev AY, Van Allen EM, Bertagnolli M, Sorger PK, Sullivan RJ,
1217 Flaherty KT, Frederick DT, Jane-Valbuena J, Yoon CH, Rozenblatt-Rosen O, Shalek AK,
1218 Regev A, Garraway LA. 2016. Dissecting the multicellular ecosystem of metastatic
1219 melanoma by single-cell RNA-seq. Science 352:189-96.
1220 62. Whitfield ML, Sherlock G, Saldanha AJ, Murray JI, Ball CA, Alexander KE, Matese JC,
1221 Perou CM, Hurt MM, Brown PO, Botstein D. 2002. Identification of genes periodically
1222 expressed in the human cell cycle and their expression in tumors. Mol Biol Cell 13:1977-
1223 2000.
1224 63. Hiyama H, Iavarone A, Reeves SA. 1998. Regulation of the cdk inhibitor p21 gene during
1225 cell cycle progression is under the control of the transcription factor E2F. Oncogene
1226 16:1513-23.

1227 64. Horne MC, Goolsby GL, Donaldson KL, Tran D, Neubauer M, Wahl AF. 1996. Cyclin G1
1228 and cyclin G2 comprise a new family of cyclins with contrasting tissue-specific and cell
1229 cycle-regulated expression. J Biol Chem 271:6050-61.
1230 65. Bostrom J, Sramkova Z, Salasova A, Johard H, Mahdessian D, Fedr R, Marks C, Medalova
1231 J, Soucek K, Lundberg E, Linnarsson S, Bryja V, Sekyrova P, Altun M, Andang M. 2017.
1232 Comparative cell cycle transcriptomics reveals synchronization of developmental
1233 transcription factor networks in cancer cells. PLoS One 12:e0188772.
1234 66. Hirose K, Kawashima T, Iwamoto I, Nosaka T, Kitamura T. 2001. MgcRacGAP is involved
1235 in cytokinesis through associating with mitotic spindle and midbody. J Biol Chem
1236 276:5821-8.
1237 67. Fontijn RD, Goud B, Echard A, Jollivet F, van Marle J, Pannekoek H, Horrevoets AJ. 2001.
1238 The human kinesin-like protein RB6K is under tight cell cycle control and is essential for
1239 cytokinesis. Mol Cell Biol 21:2944-55.
1240 68. Santos A, Wernersson R, Jensen LJ. 2015. Cyclebase 3.0: a multi-organism database on
1241 cell-cycle regulation and phenotypes. Nucleic Acids Res 43:D1140-4.
1242 69. Wolf FA, Angerer P, Theis FJ. 2018. SCANPY: large-scale single-cell gene expression data
1243 analysis. Genome Biol 19:15.
1244 70. Finak G, McDavid A, Yajima M, Deng J, Gersuk V, Shalek AK, Slichter CK, Miller HW,
1245 McElrath MJ, Prlic M, Linsley PS, Gottardo R. 2015. MAST: a flexible statistical
1246 framework for assessing transcriptional changes and characterizing heterogeneity in
1247 single-cell RNA sequencing data. Genome Biol 16:278.

1248 71. Gennady Korotkevich VS, Alexey Sergushichev. 2019. Fast gene set enrichment analysis.
1249 bioRxiv doi:https://doi.org/10.1101/060012
1250
1251
1252
1253
1254
1255
1256
1257
1258
1259
1260
1261
1262
1263
1264
1265
1266
1267
1268
1269
1270

1271 **MAIN TEXT FIGURE AND TABLE LEGENDS**

1272 **Figure 1.** Experimental pipeline. **(A)** Simplified illustration of effector secretion during
1273 early tachyzoite infection. Black curved arrows = modulation of host transcription, gray
1274 curved arrows = transitions through stages of lytic cycle, black jagged arrow =
1275 modulation without translocation to the nucleus, ROPs = rhoptry proteins, MIGs = MYR-
1276 independent dense granule proteins (GRAs), MDGs = MYR-dependent GRAs, MYR =
1277 putative translocation required for MDG penetration of host cytosol. **(B)** As a result of
1278 the events in (A), infected host cell monolayers produce infected-injected (I-I) cells when
1279 tachyzoite invasion proceeds as usual, uninfected-uninjected (U-U) bystander cells, and
1280 uninfected-injected (U-I) cells from aborted invasion after effector injection. **(C)** Pipeline
1281 to collect and analyze experimental conditions for single cell RNA sequencing. BLA =
1282 toxofilin-beta-lactamase ROP fusion protein, CCF2-AM = indicator dye that reveals
1283 injected (blue) vs. uninjected (green) cells. **(D)** FACS gating strategy to obtain mock-
1284 infected U-U, I-I, and U-I cells. **(E)** Proportion of injected (U-I + I-I) cells that are U-I. **(F)**
1285 Abundances of U-U, I-I, and U-I cells during FACS, expressed as percentages of cells
1286 from the Live/Mock gate from which they were sorted.

1287

1288 **Figure 2.** Infection response recapitulates previously identified signatures of early
1289 infection. **(A)** Gene set enrichment analysis (GSEA) of the ranked list of differentially
1290 expressed genes between Wt I-I and mock cells at 2 hpi (FDR < 0.1, FC > 1.5x) using
1291 the Hallmark gene sets from the Molecular Signatures Database. **(B)** GSEA as in (A) of
1292 the ranked differentially expressed genes between Wt I-I and mock cells at 3 hpi. FDR =

1293 false discovery rate and NES = normalized enrichment score. Gray cells indicate
1294 pathways common to those identified with FDR $<10^{-5}$ in Naor et al 2018.
1295
1296 **Figure 3.** Host response to injected parasite effectors. **(A)** GSEA of the ranked list of
1297 differentially expressed genes (FDR < 0.1, fold change > 1.5x) between Wt U-I and Wt
1298 U-U cells at 3 hpi using the Hallmark gene sets. Green rows indicate gene sets enriched
1299 from genes expressed higher in Wt U-I than in Wt U-U, and red rows indicate gene sets
1300 enriched in genes expressed lower in Wt U-I than in Wt U-U. Gene sets are designated
1301 as part of the infection response if they were also found to be enriched from DEGs
1302 between Wt I-I vs. Mock at 2 hpi or 3 hpi. **(B)** GSEA as in (A) between various U-I cells
1303 (i.e., from the Wt, CytD, and Dmyr1 infection conditions) and their cognate U-U cells at
1304 3 hpi. Gene sets in bold gray text were also found to be enriched in the infection
1305 response. Positive normalized enrichment scores represent enrichment in genes
1306 expressed higher in U-I cells than in U-U cells.
1307
1308 **Figure 4**. Comparison of host response to injection vs. infection (i.e., signatures in Wt
1309 U-I vs. Wt I-I cells.) **(A)** Scatterplot comparing injection-associated genes in Wt I-I cells
1310 and Wt U-I cells, as determined by the Spearman correlation of gene expression to the
1311 CCF2-AM ratio in Wt I-I and Wt U-I cells. Contours reflect density of points, with central
1312 contours being in the area of highest density. Labeled points on the plot are the top 20
1313 genes with the lowest probability of belonging to a Gaussian model fit with parameters
1314 that best describe the observed Spearman correlation data. *Top panels*: Plots of genes
1315 at 2 hpi. *Bottom panels*: Plots of genes at 3 hpi. *Right panels*: Schematics

1316 demonstrating regions of the scatterplots where gene expression trends in Wt U-I cells
1317 are either enhanced or counterbalanced (repressed) upon parasite penetration and
1318 release of GRA effectors into the host cell (as seen in Wt I-I cells). **(B)** GSEA of the
1319 ranked list of differentially expressed genes between Wt U-I and Wt I-I cells at 3 hpi,
1320 where green rows denote gene sets enriched from genes expressed higher in Wt U-I
1321 cells than in Wt I-I cells and red rows represent genes expressed higher in Wt I-I than in
1322 Wt U-I. FDR = false discovery rate, NES = normalized enrichment score.
1323
1324 **Figure 5**. GSEA of the ranked list of differentially expressed genes between Dmyr1 U-I
1325 and Dmyr1 I-I cells at 3 hpi, which illustrates the impact of MYR-independent GRAs and
1326 parasite penetration on the host response to infection with *Toxoplasma.* Green rows
1327 denote gene sets enriched from genes expressed higher in Dmyr1 U-I cells than in
1328 Dmyr1 I-I cells and red rows represent genes expressed higher in Dmyr1 I-I cells than in
1329 Dmyr1 U-I cells. FDR = false discovery rate, NES = normalized enrichment score.
1330
1331 **Figure 6**. Impact of MYR-dependent GRAs and MYR-dependent paracrine effectors,
1332 as illustrated by comparing Dmyr1 I-I and Wt I-I cells. **(A)** GSEA of ranked list of
1333 differentially expressed genes between Dmyr1 I-I and Wt I-I cells at 3 hpi. Green rows
1334 denote enrichment from genes expressed higher in Dmyr1 I-I cells than in Wt I-I cells,
1335 and red rows represent enrichment from genes expressed higher in Wt I-I than in Wt U-I.
1336 FDR = false discovery rate, NES = normalized enrichment score. **(B)** Scatterplot
1337 comparing injection-associated genes in Dmyr1 I-I cells and Wt I-I cells, as determined
1338 by the Spearman correlation of gene expression to the CCF2-AM ratio in Dmyr1 I-I and

1339 Wt I-I cells. Contours reflect density of points, with central contours being in the area of
1340 highest density. Labeled points on the plot are the top 20 genes with the lowest
1341 probability of belonging to a Gaussian model fit with parameters that best describe the
1342 observed Spearman correlation data. *Top panels*: Plots of genes at 2 hpi. *Bottom*
1343 *panels*: Plots of genes at 3 hpi. *Right panels*: Schematics demonstrating regions of the
1344 scatterplots where gene expression trends in Dmyr1 I-I cells are either enhanced or
1345 counterbalanced (repressed) by MYR-dependent GRAs or paracrine effects (as seen in
1346 Wt I-I cells).
1347
1348 **Figure 7.** Comparison of Dmyr1 U-U vs. Mock cell types reveals impact of MYR-
1349 dependent paracrine effects on host cell transcription during *Toxoplasma* infection. **(A)**
1350 GSEA of the ranked list of differentially expressed genes between Dmyr1 U-U and Mock
1351 cells at 3 hpi. FDR = false discovery rate, NES = normalized enrichment score, and sc =
1352 the current single cell RNA-seq dataset. **(B)** Trends in expression of Dmyr1 U-U vs.
1353 Mock DEGs are preserved in U-I and I-I cells from Wt and Dmyr1 infections, as
1354 illustrated by strip plots depicting expression of DEGs between Dmyr1 U-U and Mock
1355 cells across all cell types. Each point represents a single cell, and its y-axis
1356 displacement reflects the average of the normalized expression scores for all DEGs
1357 between Dmyr1 U-U and Mock cells. The normalized expression score of a given gene
1358 is calculated by scaling the $\log_2$ count per median (cpm) for that gene, such that the cell
1359 with the lowest cpm receives a score of 0, and the cell with the highest cpm receives a
1360 score of 1.
1361

1362 **Figure 8.** Summary of host transcriptional response to parasite-dependent stimuli. **(A)**
1363 Bubble plot of parasite-dependent host transcriptional signatures at 3 hpi that depicts
1364 the behavior of 11 representative Hallmark gene sets from the Molecular Signatures
1365 Database (columns) across 8 key comparisons between experimental conditions (rows,
1366 indicated on left of each plot) that each encapsulates the impact of certain parasite-
1367 dependent stimuli on the 11 gene sets (indicated on right of each plot). Colors indicate
1368 normalized enrichment scores (NES) from GSEA of differentially expressed genes
1369 (DEGs) between each comparison. FDR = false discovery rate, where FDR < 0.25 is
1370 considered significant (as is standard for GSEA). Parasite-dependent stimuli include
1371 ROPs = rhoptry proteins, MDGs = MYR-dependent dense granule proteins (GRAs),
1372 MIGs = MYR-independent GRAs, P = paracrine effects (where MD = MYR-dependent
1373 and MI = MYR-independent), and All = ROPs + MDGs + MIGs + Parasite penetration +
1374 P. **(B)** Bubble plot as in (A) where colors indicate log2 normalized fold change in
1375 expression of DEGs that fall under each comparison and each gene set. **(C)** Model of
1376 individual impacts of parasite-dependent stimuli on host transcription, which include
1377 immune pathways (e.g., TNFA Signaling via NFKB, IL6 JAK STAT3 Signaling,
1378 Inflammatory Response, IL2 STAT5 Signaling, Interferon Gamma Response, and
1379 Allograft Rejection), cellular stress (e.g., Hypoxia, Apoptosis), and cell proliferation-
1380 associated pathways (i.e., KRAS signaling, p53 pathway). Curved lines indicate
1381 modulation of host transcription, and jagged lines indicate modulation without effector
1382 translocation to the nucleus.
1383

1384 **Table 1.** Parasite-derived stimuli (with an emphasis on effectors) to which cells from
1385 each experimental condition responds, according to the current model of effector
1386 secretion for *Toxoplasma* tachyzoites. ROPs = rhoptry proteins, GRAs = dense granule
1387 proteins, PV = parasitophorous vacuole. The "wild type" and "mutant" designations for
1388 paracrine effectors reflect potential differences in paracrine effectors from monolayers
1389 infected with wild type vs. *Δmyr1* parasites.
1390

1391 **SUPPLEMENTARY FILE FIGURE AND TABLE LEGENDS**

1392 **Figure S1.** Human foreskin fibroblast (HFF) feeder cell debris contaminates the
1393 uninfected-injected (U-I) FACS gate. In all panels, a host cell monolayer is treated with
1394 either a parasite-free lysate of HFFs or RH Tfn-HA-BLA parasites syringe released from
1395 HFFs and then incubated with CCF2-AM to reveal (un)injected cells. *Left:* Infection with
1396 RH Tfn-HA-BLA reveals uninjected and injected cell populations. *Middle:* Mock
1397 "infection" with para- site-free lysate reveals HFF feeder cell debris contaminating the
1398 "injected" cell population. *Right:* Infection with parasite-free lysate that was washed to
1399 remove HFF debris reveals a reduction in contamination of the injected population.
1400

1401 **Figure S2. (A)** Serum starvation for 24 h partially inhibits cell division of 10 T1/2 host
1402 cells, reducing the possibility of capturing U-I cells that arise from division of an infected
1403 host cell (U-Id cells) rather than from an aborted invasion event. Note that the S phase
1404 population in the bottom right panel (serum replete, infected cells) also contains G1
1405 phase cells containing parasites, as parasite nuclear content enhances the propidium
1406 iodide signal in these cells. **(B)** Histogram depicting the number of infected host cells

1407 that divided at various times post-infection, as determined by live video microscopy
1408 footage of 200 serum starved 10 T1/2 cells for which the precise moment of infection
1409 was captured on camera. Of the 200 infected 10 T1/2 cells, 53 divided over a 16 hour
1410 time course, and none divided at earlier than 3.67 hours post-infection.
1411
1412 **Figure S3**. Quality control metrics for single cell RNA sequencing data. **(A)** Comparison
1413 of gene counts (number of genes for which reads from each cell mapped to the
1414 concatenated mouse-*Toxoplasma* genome, y-axis) and read sum (total reads, x-axis)
1415 for all experimental trials. Cells that passed quality control are indicated in color. **(B)**
1416 Percentages of total reads that mapped to open reading frames (ORFs) in the mouse-
1417 *Toxoplasma* concatenated genome. **(C)** *Top panel:* Linear regression modeling of
1418 measurement accuracy fitted on ERCC spike-ins with abundance above the detection
1419 limit. The text within each subplot denotes the coefficient of determination for the
1420 regression fit. *Bottom panel:* Logistic regression modeling of detection limit based on
1421 ERCC spike-ins. The 50% detection rate is indicated with a black dotted line, and the
1422 text within each subplot indicates the detection limit for each experiment in absolute
1423 molecular counts. **(D)** Linear regression fitted to scatterplot of average gene counts of
1424 differentially expressed genes for single cell RNA sequencing data (x-axis) vs. bulk RNA
1425 sequencing data (y-axis). Each point represents a DEG. Text within each subplot
1426 denotes the coefficient of determination (R^2) for the regression. **(E)** The coefficients of
1427 determination for linear regression lines fit to scatterplots as in (D) for all possible
1428 combinations of single vs. bulk RNA-seq combinations.
1429

1430 **Figure S3**. Quality control metrics for single cell RNA sequencing data. **(A)** Comparison
1431 of gene counts (number of genes for which reads from each cell mapped to the
1432 concatenated mouse-*Toxoplasma* genome, y-axis) and read sum (total reads, x-axis)
1433 for all experimental trials. Cells that passed quality control are indicated in color. **(B)**
1434 Percentages of total reads that mapped to open reading frames (ORFs) in the mouse-
1435 *Toxoplasma* concatenated genome. **(C)** *Top panel:* Linear regression modeling of
1436 measurement accuracy fitted on ERCC spike-ins with abundance above the detection
1437 limit. The text within each subplot denotes the coefficient of determination for the
1438 regression fit. *Bottom panel:* Logistic regression modeling of detection limit based on
1439 ERCC spike-ins. The 50% detection rate is indicated with a black dotted line, and the
1440 text within each subplot indicates the detection limit for each experiment in absolute
1441 molecular counts. **(D)** Linear regression fitted to scatterplot of average gene counts of
1442 differentially expressed genes for single cell RNA sequencing data (x-axis) vs. bulk RNA
1443 sequencing data (y-axis). Each point represents a DEG. Text within each subplot
1444 denotes the coefficient of determination (R^2) for the regression. **(E)** The coefficients of
1445 determination for linear regression lines fit to scatterplots as in (D) for all possible
1446 combinations of single vs. bulk RNA-seq combinations.
1447
1448 **Figure S4.** Single cell resolution enables strategic partitioning of individual cells for
1449 downstream analysis. **(A)** Percentage of reads derived from *Toxoplasma* validates
1450 infection status of individual cells. Cells are scored as uninfected if left of the lower
1451 decision line (bold, dashed), infected if right of the upper decision line (dotted), and
1452 ambiguous if between the decision lines (cross-hatched section). **(B)** Principal

1453 component analysis (PCA) projection of cells based on 175 curated cell cycle markers
1454 and subsequent Leiden clustering enables partitioning of cells by predicted cell cycle
1455 states, G1 (green), S (gold), and G2/M (purple). **(C)** Proportion of cells from each
1456 experimental condition in each cell cycle phase. **(D)** Dimensionality reduction and
1457 projection of single cells using the *Uniform Manifold Approximation and Projection*
1458 (UMAP) algorithm reveals 3 putative cell populations. All panels are reproduced copies
1459 of the same projection, each of which is color coded by specific parameters. *Left:*
1460 Louvain clusters, used to assign the cells to populations 1, 2, and 3; *middle:* cell cycle
1461 phase; *right (3 panels):* experimental trial (1 hpi, 2 hpi, and 3 hpi).
1462
1463 **Figure S5.** Construction and validation of RH Δmyr1 mCherry Toxofilin-HA-beta-
1464 lactamase (RH Δmyr1 mCherry Tfn-HA-BLA). **(A)** CRISPR/Cas9 strategy to construct
1465 RH Δmyr1 mCherry Tfn-HA-BLA by disrupting parasite UPRT (blue) in parental strain
1466 RH Δmyr1 mCherry. The parental strain was transfected with plasmid pSAG1::Cas9-
1467 U6::sgUPRT (pink) and a linear amplicon containing Tfn-HA-BLA (purple) and flanked
1468 with 20 nucleotide homology arms to UPRT (blue). The region of UPRT complementary
1469 to the guide RNA, which also contains the site at which Cas9 cleaves, is in pink. **(B)**
1470 Western blot for the Tfn-HA-BLA construct in RH Δmyr1 mCherry Tfn-HA-BLA. All lanes
1471 were obtained from the same gel. **(C)** Immunofluorescence assay (IFA) for
1472 colocalization of the Tfn-HA-BLA protein product and ROP2/3/4. **(D)** FACS analysis of
1473 10 T1/2 cells infected with parasite-free lysate, RH Tfn-HA-BLA, and RH Δmyr1
1474 mCherry Tfn-HA-BLA. Cleavage of reporter dye CCF2-AM indicates injection of the Tfn-
1475 HA-BLA construct.

1476

1477 **Table S1:** Mouse genes discarded due to reads from extracellular RH parasites

1478 mapping to these genes in the concatenated mouse-*Toxoplasma* genome

1479

1480 **Table S2:** Curated list of genes used to assign cell cycle phases to single host cells

1481

1482 **Table S3:** Differentially expressed genes (DEGs). In all tables, fdr = false discovery rate,

1483 and log2FC is the $\log_2$ fold change in expression of DEGs between the indicated

1484 conditions. **(A)** All differentially expressed genes at all time points. **(B)** Wt I-I vs. Mock

1485 Differentially Expressed Genes. **(C)** Wt U-I vs. Wt U-U Differentially Expressed Genes.

1486 **(D)** Dmyr1 U-I vs. Dmyr1 U-U Differentially Expressed Genes. **(E)** CytD U-I vs. CytD U-

1487 U Differentially Expressed Genes. **(F)** Wt U-I vs. Wt I-I Differentially Expressed Genes.

1488 **(G)** Dmyr1 U-I vs. Dmyr1 I-I Differentially Expressed Genes. **(H)** Wt I-I vs. Dmyr1 I-I

1489 Differentially Expressed Genes. **(I)** Wt U-U vs. Mock Differentially Expressed Genes. **(J)**

1490 Dmyr1 U-U vs. Mock Differentially Expressed Genes. For (F) and (G), a gene is

1491 designated as showing evidence of being acted upon by counterbalancing effectors

1492 (indicated in the "Evidence of Effector Counterbalancing?" column) if it exhibits either: 1)

1493 upregulation in one cell type and downregulation in the other compared to a common

1494 Wt U-U standard, or 2) more upregulation or downregulation in Wt U-I cells compared to

1495 the standard than in Wt I-I cells.

1496

1497 **Table S4:** CCF2-AM correlation data for **(A)** Wt U-I vs. Wt I-I cells and **(B)** Dmyr1 I-I vs.

1498 Wt I-I cells. A gene is designated as showing evidence of being acted upon by

1499 counterbalancing effectors (indicated under the “Evidence of Effector

1500 Counterbalancing?” column) if it exhibits either: 1) negative correlation with CCF2-AM in

1501 one cell type and a positive CCF2-AM correlation in the other cell type, or 2) stronger

1502 positive or negative correlations in Wt U-I cells than in Wt I-I cells.

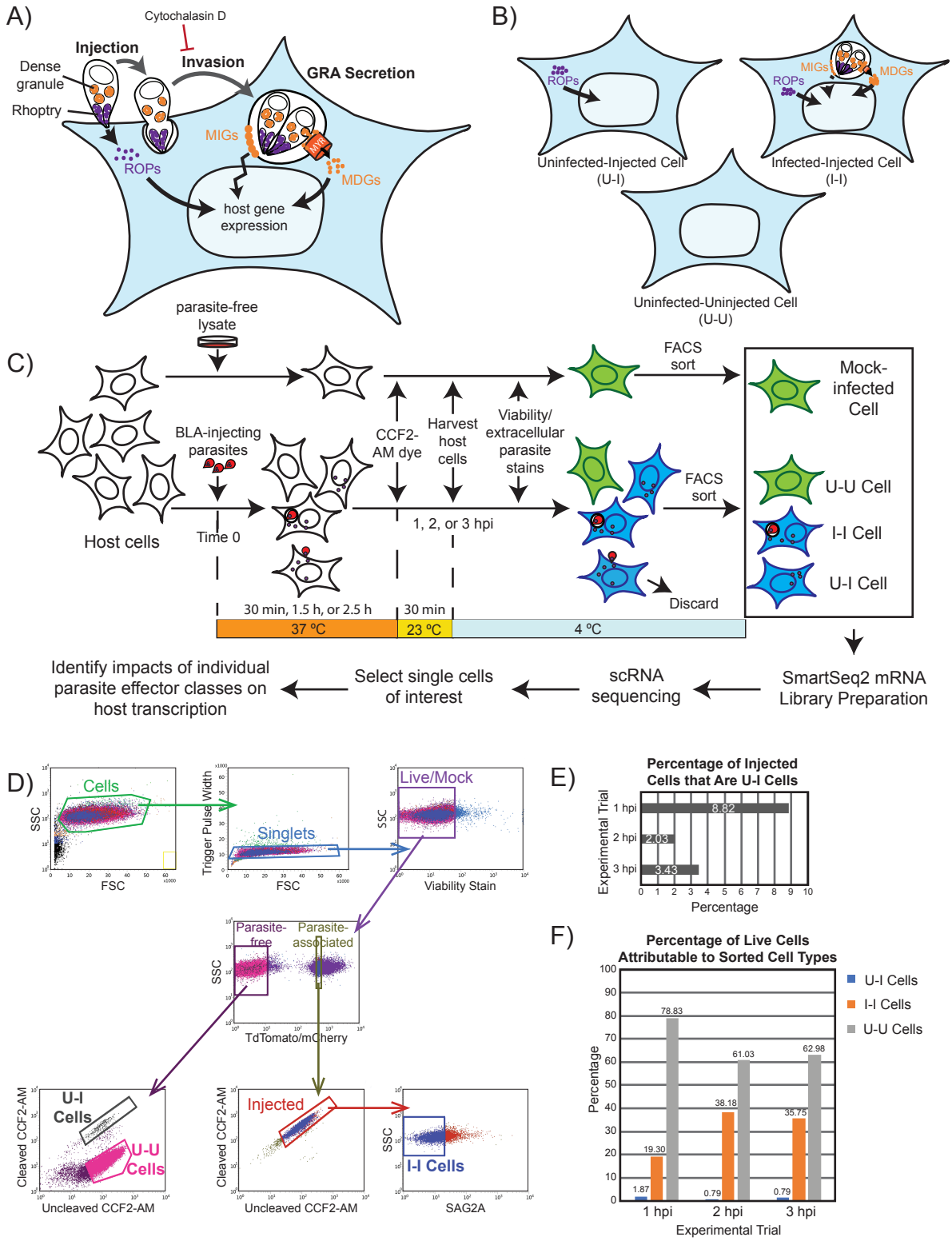

Figure 1. Experimental pipeline. **(A)** Simplified illustration of effector secretion during early tachyzoite infection. Black curved arrows = modulation of host transcription, gray curved arrows = transitions through stages of lytic cycle, black jagged arrow = modulation without translocation to the nucleus, ROPs = rhoptry proteins, MIGs = MYR-independent dense granule proteins (GRAs), MDGs = MYR-dependent GRAs, MYR = putative translocation required for MDG penetration of host cytosol. **(B)** As a result of the events in (A), infected host cell monolayers produce infected-injected (I-I) cells when tachyzoite invasion proceeds as usual, uninfected-uninjected (U-U) bystander cells, and uninfected-injected (U-I) cells from aborted invasion after effector injection. **(C)** Pipeline to collect and analyze experimental conditions for single cell RNA sequencing. BLA = toxofilin-beta-lactamase ROP fusion protein, CCF2-AM = indicator dye that reveals injected (blue) vs. uninjected (green) cells. **(D)** FACS gating strategy to obtain mock-infected U-U, I-I, and U-I cells. **(E)** Proportion of injected (U-I + I-I) cells that are U-I. **(F)** Abundances of U-U, I-I, and U-I cells during FACS, expressed as percentages of cells from the Live/Mock gate from which they were sorted.

A)

Wt I-I vs mock GSEA (2 hpi)

	Gene Set	FDR	NES	Identified at 6 hpi (Naor et al 2018)
Higher in Wt I-I	TNFA SIGNALING VIA NFKB	0.078	1.888	Yes
	ALLOGRAFT REJECTION	0.086	1.634	Yes
	IL6 JAK STAT3 SIGNALING	0.108	1.692	Yes
	INTERFERON GAMMA RESPONSE	0.108	1.785	Yes
	ESTROGEN RESPONSE LATE	0.169	1.573	Yes
Higher in Mock	TGF BETA SIGNALING	0.199	-1.725	No
	UV RESPONSE DN	0.199	-1.594	Yes

B)

Wt I-I vs mock GSEA (3 hpi)

	Gene Set	FDR	NES	Identified at 6 hpi (Naor et al 2018)
Higher in Wt I-I	TNFA SIGNALING VIA NFKB	0.052	2.596	Yes
	INFLAMMATORY RESPONSE	0.052	2.065	Yes
	ALLOGRAFT REJECTION	0.052	2.062	Yes
	IL6 JAK STAT3 SIGNALING	0.052	1.997	Yes
	APOPTOSIS	0.059	1.85	Yes
	P53 PATHWAY	0.059	1.762	Yes
	IL2 STAT5 SIGNALING	0.071	1.803	Yes
	KRAS SIGNALING DN	0.089	1.703	Yes
	INTERFERON GAMMA RESPONSE	0.103	1.729	Yes
	UV RESPONSE DN	0.148	1.669	Yes
	UV RESPONSE UP	0.159	1.565	Yes
	HEME METABOLISM	0.163	1.574	Yes
	MTORC1 SIGNALING	0.163	1.525	Yes
	MITOTIC SPINDLE	0.185	1.504	No
	E2F TARGETS	0.243	1.458	Yes
Higher in Mock	APICAL SURFACE	0.052	-1.636	No
	OXIDATIVE PHOSPHORYLATION	0.052	-2.191	No
	KRAS SIGNALING UP	0.154	-1.639	No
	COAGULATION	0.159	-1.592	No
	ANGIOGENESIS	0.159	-1.602	No
	MYOGENESIS	0.163	-1.638	Yes

Figure 2. Infection response recapitulates previously identified signatures of early infection. **(A)** Gene set enrichment analysis (GSEA) of the ranked list of differentially expressed genes between Wt I-I and mock cells at 2 hpi (FDR < 0.1, FC > 1.5x) using the Hallmark gene sets from the Molecular Signatures Database. **(B)** GSEA as in (A) of the ranked differentially expressed genes between Wt I-I and mock cells at 3 hpi. FDR = false discovery rate and NES = normalized enrichment score. Gray cells indicate pathways common to those identified with FDR $<10^{-5}$ in Naor et al 2018.

A)

GSEA for Wt U-I vs. Wt U-U at 3 hpi

	Gene Set	FDR	NES	Part of Infection Response?
Higher in Wt U-I	TNFA SIGNALING VIA NFKB	0.019	2.699	Yes
	INFLAMMATORY RESPONSE	0.019	2.483	Yes
	KRAS SIGNALING UP	0.019	2.113	No
	IL6 JAK STAT3 SIGNALING	0.019	2.021	Yes
	HYPOXIA	0.058	1.842	No
	IL2 STAT5 SIGNALING	0.06	1.823	Yes
	ALLOGRAFT REJECTION	0.06	1.809	Yes
	EPITHELIAL MESENCHYMAL TRANSITION	0.06	1.787	No
	INTERFERON GAMMA RESPONSE	0.06	1.766	Yes
	P53 PATHWAY	0.064	1.74	Yes
	COMPLEMENT	0.142	1.578	No
	KRAS SIGNALING DN	0.121	1.541	Yes
	APICAL JUNCTION	0.159	1.524	No
	UV RESPONSE DN	0.192	1.491	Yes
Higher in Wt U-U	NOTCH SIGNALING	0.115	-1.323	No
	UNFOLDED PROTEIN RESPONSE	0.216	-1.416	No
	OXIDATIVE PHOSPHORYLATION	0.075	-1.771	Yes

B)

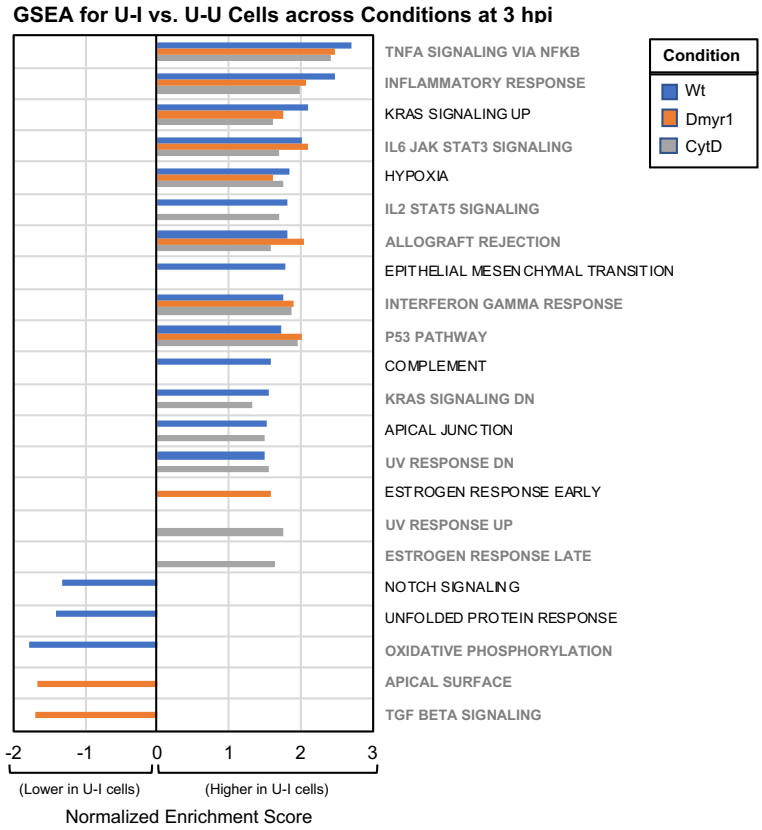

Figure 3. Host response to injected parasite effectors. **(A)** GSEA of the ranked list of differentially expressed genes (FDR < 0.1, fold change > 1.5x) between Wt U-I and Wt U-U cells at 3 hpi using the Hallmark gene sets. Green rows indicate gene sets enriched from genes expressed higher in Wt U-I than in Wt U-U, and red rows indicate gene sets enriched in genes expressed lower in Wt U-I than in Wt U-U. Gene sets are designated as part of the infection response if they were also found to be enriched from DEGs between Wt I-I vs. Mock at 2 hpi or 3 hpi. **(B)** GSEA as in (A) between various U-I cells (i.e., from the Wt, CytD, and Dmyr1 infection conditions) and their cognate U-U cells at 3 hpi. Gene sets in bold gray text were also found to be enriched in the infection response. Positive normalized enrichment scores represent enrichment in genes expressed higher in U-I cells than in U-U cells.

A)

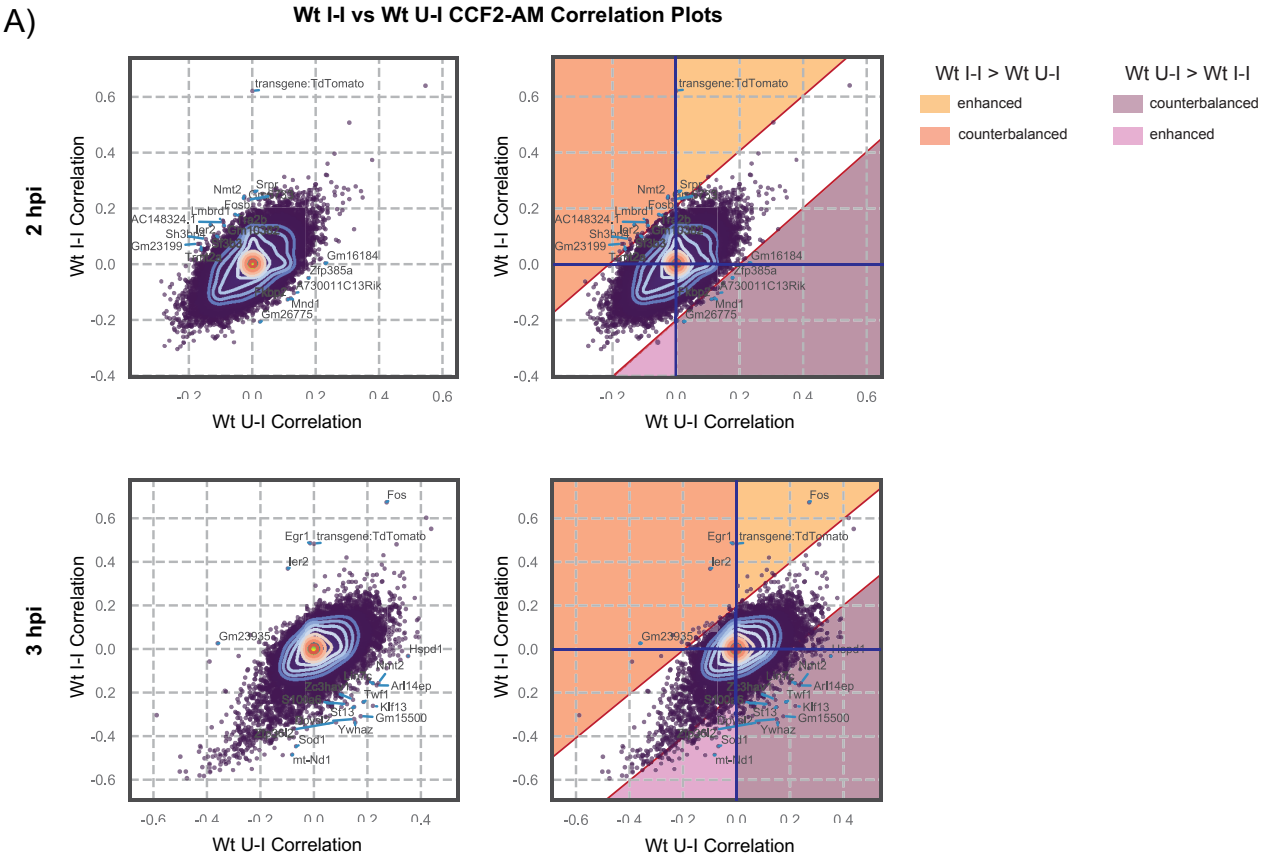

B)

GSEA for Wt U-I vs. Wt I-I at 3 hpi

	Gene Set	FDR	NES
Higher in Wt U-I	EPITHELIAL MESENCHYMAL TRANSITION	0.050	2.029
	MYOGENESIS	0.050	1.893
	COMPLEMENT	0.054	1.854
	COAGULATION	0.092	1.736
	PI3K AKT MTOR SIGNALING	0.100	1.645
	BILE ACID METABOLISM	0.100	1.574
	XENOBIOTIC METABOLISM	0.198	1.505
	ANDROGEN RESPONSE	0.198	1.487
	KRAS SIGNALING DN	0.198	1.407
	ANGIOGENESIS	0.232	1.334
Higher in Wt I-I	UV RESPONSE UP	0.05	-2.165
	TNFA SIGNALING VIA NFKB	0.081	-1.855
	IL6 JAK STAT3 SIGNALING	0.092	-1.934
	ALLOGRAFT REJECTION	0.100	-1.847
	ESTROGEN RESPONSE EARLY	0.186	-1.593
	INTERFERON GAMMA RESPONSE	0.186	-1.627
	ESTROGEN RESPONSE LATE	0.186	-1.636
	MITOTIC SPINDLE	0.232	-1.458

Figure 4. Comparison of host response to injection vs. infection (i.e., signatures in Wt U-I vs. Wt I-I cells.) **(A)** Scatterplot comparing injection-associated genes in Wt I-I cells and Wt U-I cells, as determined by the Spearman correlation of gene expression to the CCF2-AM ratio in Wt I-I and Wt U-I cells. Contours reflect density of points, with central contours being in the area of highest density. Labeled points on the plot are the top 20 genes with the lowest probability of belonging to a Gaussian model fit with parameters that best describe the observed Spearman correlation data. *Top panels*: Plots of genes at 2 hpi. *Bottom panels*: Plots of genes at 3 hpi. *Right panels*: Schematics demonstrating regions of the scatterplots where gene expression trends in Wt U-I cells are either enhanced or counterbalanced (repressed) upon parasite penetration and release of GRA effectors into the host cell (as seen in Wt I-I cells). **(B)** GSEA of the ranked list of differentially expressed genes between Wt U-I and Wt I-I cells at 3 hpi, where green rows denote gene sets enriched from genes expressed higher in Wt U-I cells than in Wt I-I cells and red rows represent genes expressed higher in Wt I-I than in Wt U-I. FDR = false discovery rate, NES = normalized enrichment score.

Cell Type	Impinging Parasite-Derived Stimuli				
Mock	-	-	-	-	-
Wt U-U	Paracrine (wild type)	-	-	-	-
Wt U-I	Paracrine (wild type)	ROPs	-	-	-
Wt I-I	Paracrine (wild type)	ROPs	MYR-independent GRAs	MYR-dependent GRAs	Internalized Parasite/PV
Dmyr1 U-U	Paracrine (mutant)	-	-	-	-
Dmyr1 U-I	Paracrine (mutant)	ROPs	-	-	-
Dmyr1 I-I	Paracrine (mutant)	ROPs	MYR-independent GRAs	-	Internalized Parasite/PV

Table 1. Parasite-derived stimuli (with an emphasis on effectors) to which cells from each experimental condition responds, according to the current model of effector secretion for *Toxoplasma* tachyzoites. ROPs = rhoptry proteins, GRAs = dense granule proteins, PV = parasitophorous vacuole. The “wild type” and “mutant” designations for paracrine effectors reflect potential differences in paracrine effectors from monolayers infected with wild type vs. *Δmyr1* parasites.

GSEA for Dmyr1 U-I vs. Dmyr1 I-I at 3 hpi

	Gene Set	FDR	NES	Part of Infection Response?	Part of Injection Response?	Differentially Regulated between Wt I-I and Wt U-I?
Higher in Dmyr1 U-I	COMPLEMENT	0.203	1.427	No	No	Yes
	COAGULATION	0.203	1.427	Yes	No	Yes
	MTORC1 SIGNALING	0.214	1.542	No	No	No
	MYOGENESIS	0.217	1.404	Yes	No	Yes
Higher in Dmyr1 I-I	IL6 JAK STAT3 SIGNALING	0.093	-1.900	Yes	Yes	Yes
	ALLOGRAFT REJECTION	0.126	-1.780	Yes	Yes	Yes
	UV RESPONSE UP	0.126	-1.806	Yes	No	Yes
	INTERFERON GAMMA RESPONSE	0.135	-1.711	Yes	Yes	Yes
	INFLAMMATORY RESPONSE	0.135	-1.738	Yes	Yes	No
	UV RESPONSE DN	0.135	-1.770	Yes	Yes	No
	TNFA SIGNALING VIA NFKB	0.135	-1.830	Yes	Yes	Yes
	P53 PATHWAY	0.189	-1.626	Yes	Yes	No
	KRAS SIGNALING DN	0.203	-1.335	Yes	Yes	No
	ESTROGEN RESPONSE EARLY	0.221	-1.497	No	Yes?	Yes
	ANGIOGENESIS	0.242	-1.312	No	No	No

Figure 5. GSEA of the ranked list of differentially expressed genes between Dmyr1 U-I and Dmyr1 I-I cells at 3 hpi, which illustrates the impact of MYR-independent GRAs and parasite penetration on the host response to infection with *Toxoplasma.* Green rows denote gene sets enriched from genes expressed higher in Dmyr1 U-I cells than in Dmyr1 I-I cells and red rows represent genes expressed higher in Dmyr1 I-I cells than in Dmyr1 U-I cells. FDR = false discovery rate, NES = normalized enrichment score.

A)

GSEA for Dmyr1 I-I vs. Wt I-I at 3 hpi

	Gene Set	FDR	NES	Identified at 6 hpi (Naor et al 2018)	Part of Infection Response	Part of Injection Response
Higher in Dmyr1 I-I	KRAS SIGNALING UP	0.079	2.223	No	No	Yes
	IL2 STAT5 SIGNALING	0.080	2.000	Yes	Yes	Yes
	TNFA SIGNALING VIA NFKB	0.080	1.917	Yes	Yes	Yes
	INFLAMMATORY RESPONSE	0.080	1.891	Yes	Yes	Yes
	ANGIOGENESIS	0.080	1.852	No	No	No
	PI3K AKT MTOR SIGNALING	0.080	1.826	No	No	No
	INTERFERON GAMMA RESPONSE	0.080	1.821	Yes	Yes	Yes
	APOPTOSIS	0.119	1.710	Yes	Yes	No
	IL6 JAK STAT3 SIGNALING	0.083	1.706	Yes	Yes	Yes
	COMPLEMENT	0.153	1.589	No	No	Yes
	GLYCOLYSIS	0.169	1.563	No	No	No
	HYPOXIA	0.153	1.517	Yes	No	Yes
	WNT BETA CATENIN SIGNALING	0.080	1.516	No	No	No
	HEDGEHOG SIGNALING	0.169	1.511	No	No	No
	NOTCH SIGNALING	0.169	1.504	No	No	No
Higher in Wt I-I	MITOTIC SPINDLE	0.124	-1.635	Yes	No	No

B)

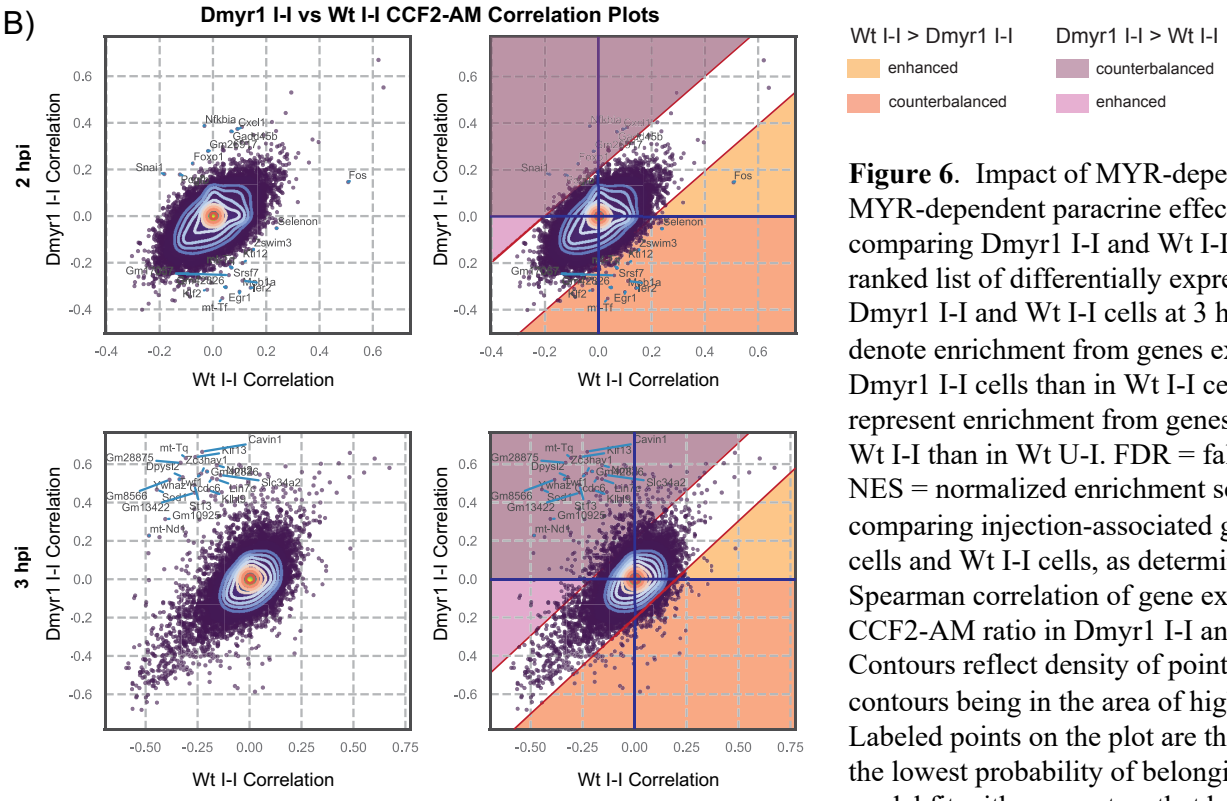

Figure 6. Impact of MYR-dependent GRAs and MYR-dependent paracrine effectors, as illustrated by comparing Dmyr1 I-I and Wt I-I cells. **(A)** GSEA of ranked list of differentially expressed genes between Dmyr1 I-I and Wt I-I cells at 3 hpi. Green rows denote enrichment from genes expressed higher in Dmyr1 I-I cells than in Wt I-I cells, and red rows represent enrichment from genes expressed higher in Wt I-I than in Wt U-I. FDR = false discovery rate, NES = normalized enrichment score. **(B)** Scatterplot comparing injection-associated genes in Dmyr1 I-I cells and Wt I-I cells, as determined by the Spearman correlation of gene expression to the CCF2-AM ratio in Dmyr1 I-I and Wt I-I cells. Contours reflect density of points, with central contours being in the area of highest density. Labeled points on the plot are the top 20 genes with the lowest probability of belonging to a Gaussian model fit with parameters that best describe the observed Spearman correlation data. *Top panels*: Plots of genes at 2 hpi. *Bottom panels*: Plots of genes at 3 hpi. *Right panels*: Schematics demonstrating regions of the scatterplots where gene expression trends in Dmyr1 I-I cells are either enhanced or counterbalanced (repressed) by MYR-dependent GRAs or paracrine effects (as seen in Wt I-I cells).

A)

GSEA for Dmyr1 U-U vs. Mock at 3 hpi

	Gene Set	FDR	NES	Part of Infection Response (sc)	Part of Infection Response (Naor et al 2018)	Part of Injection Response (sc)
Higher in Dmyr1 U-U than in Mock	TNFA SIGNALING VIA NFKB	0.012	2.557	Yes	Yes	Yes
	HYPOXIA	0.012	2.000	No	Yes	Yes
	IL6 JAK STAT3 SIGNALING	0.012	2.070	Yes	Yes	Yes
	INFLAMMATORY RESPONSE	0.012	2.304	Yes	Yes	Yes
	P53 PATHWAY	0.012	2.100	Yes	Yes	Yes
	KRAS SIGNALING UP	0.012	2.143	Yes (downregulated)	Yes	Yes
	CHOLESTEROL HOMEOSTASIS	0.026	1.834	No	Yes	No
	ALLOGRAFT REJECTION	0.026	1.783	Yes	Yes	Yes
	APOPTOSIS	0.029	1.790	Yes	Yes	No
	MTORC1 SIGNALING	0.029	1.741	Yes	Yes	No
	INTERFERON GAMMA RESPONSE	0.044	1.733	Yes	Yes	Yes
	XENOBIOTIC METABOLISM	0.046	1.726	No	Yes	No
	UV RESPONSE DN	0.046	1.682	Yes	Yes	Yes
	IL2 STAT5 SIGNALING	0.104	1.617	Yes	Yes	Yes
	GLYCOLYSIS	0.133	1.540	No	Yes	No
	ESTROGEN RESPONSE EARLY	0.164	1.487	No	Yes	No
	MYC TARGETS V2	0.164	1.533	No	Yes	No
	MYOGENESIS	0.192	1.483	Yes (downregulated)	Yes	No
	PI3K AKT MTOR SIGNALING	0.199	1.444	No	No	No
	UV RESPONSE UP	0.247	1.418	Yes	Yes	Yes

B)

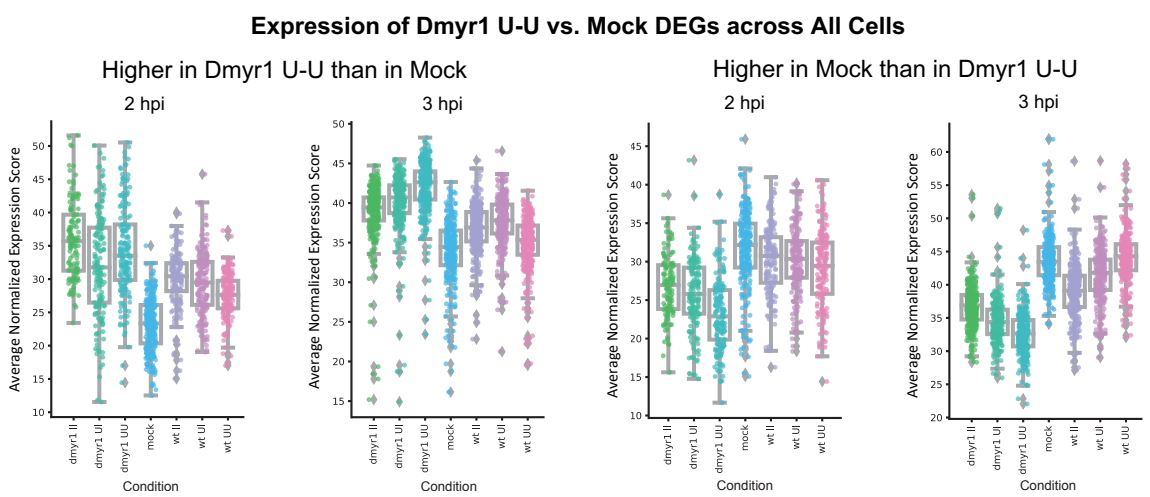

Figure 7. Comparison of Dmyr1 U-U vs. Mock cell types reveals impact of MYR-dependent paracrine effects on host cell transcription during *Toxoplasma* infection. **(A)** GSEA of the ranked list of differentially expressed genes between Dmyr1 U-U and Mock cells at 3 hpi. FDR = false discovery rate, NES = normalized enrichment score, and sc = the current single cell RNA-seq dataset. **(B)** Trends in expression of Dmyr1 U-U vs. Mock DEGs are preserved in U-I and I-I cells from Wt and Dmyr1 infections, as illustrated by strip plots depicting expression of DEGs between Dmyr1 U-U and Mock cells across all cell types. Each point represents a single cell, and its y-axis displacement reflects the average of the normalized expression scores for all DEGs between Dmyr1 U-U and Mock cells. The normalized expression score of a given gene is calculated by scaling the $\log_2$ count per median (cpm) for that gene, such that the cell with the lowest cpm receives a score of 0, and the cell with the highest cpm receives a score of 1.

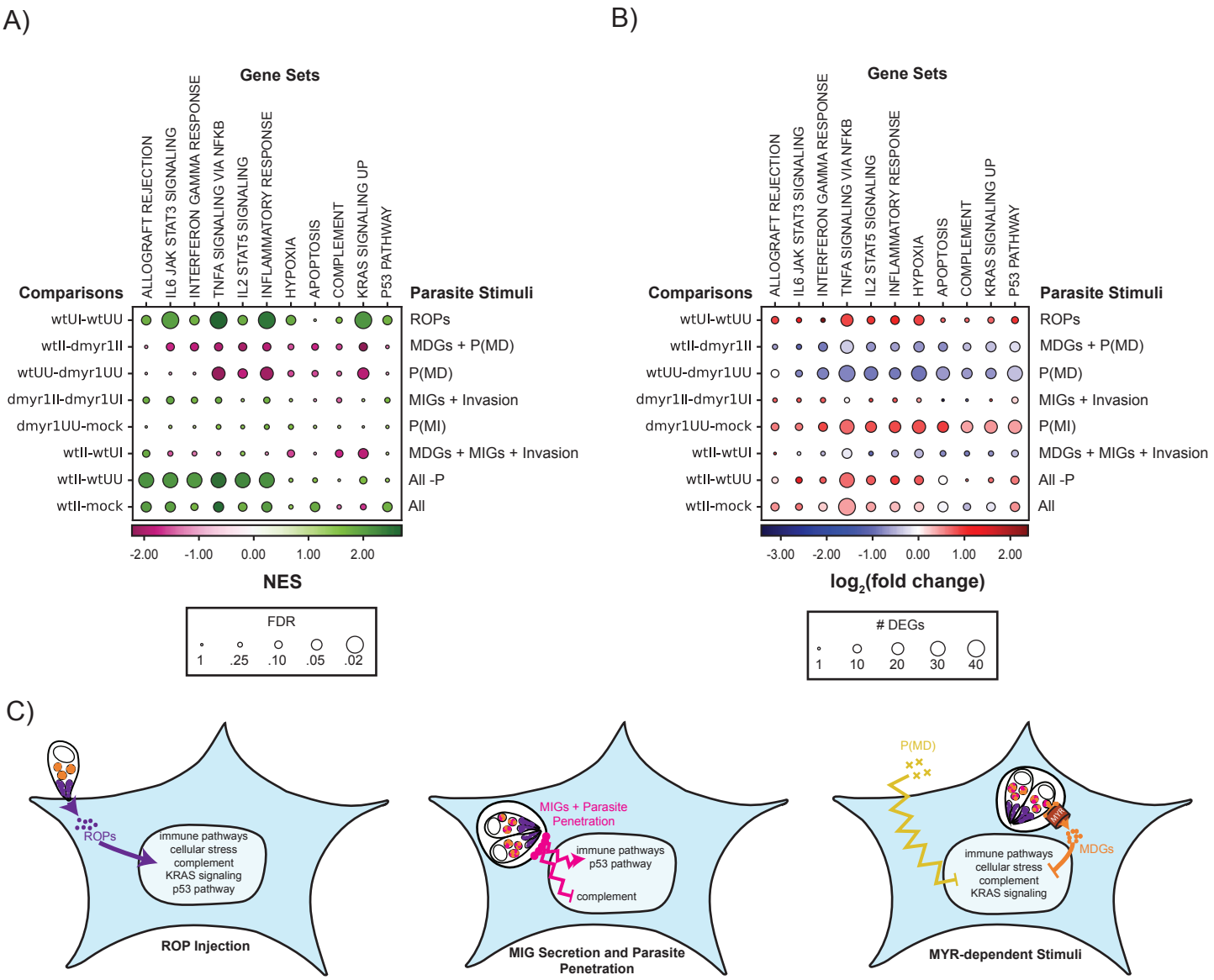

Figure 8. Summary of host transcriptional response to parasite-dependent stimuli. **(A)** Bubble plot of parasite-dependent host transcriptional signatures at 3 hpi that depicts the behavior of 11 representative Hallmark gene sets from the Molecular Signatures Database (columns) across 8 key comparisons between experimental conditions (rows, indicated on left of each plot) that each encapsulates the impact of certain parasite-dependent stimuli on the 11 gene sets (indicated on right of each plot). Colors indicate normalized enrichment scores (NES) from GSEA of differentially expressed genes (DEGs) between each comparison. FDR = false discovery rate, where FDR < 0.25 is considered significant (as is standard for GSEA). Parasite-dependent stimuli include ROPs = rhoptry proteins, MDGs = MYR-dependent dense granule proteins (GRAs), MIGs = MYR-independent GRAs, P = paracrine effects (where MD = MYR-dependent and MI = MYR-independent), and All = ROPs + MDGs + MIGs + Parasite penetration + P. **(B)** Bubble plot as in (A) where colors indicate $\log_2$ normalized fold change in expression of DEGs that fall under each comparison and each gene set. **(C)** Model of individual impacts of parasite-dependent stimuli on host transcription, which include immune pathways (e.g., TNFA Signaling via NFKB, IL6 JAK STAT3 Signaling, Inflammatory Response, IL2 STAT5 Signaling, Interferon Gamma Response, and Allograft Rejection), cellular stress (e.g, Hypoxia, Apoptosis), and cell proliferation-associated pathways (i.e., KRAS signaling, p53 pathway). Curved lines indicate modulation of host transcription, and jagged lines indicate modulation without effector translocation to the nucleus.

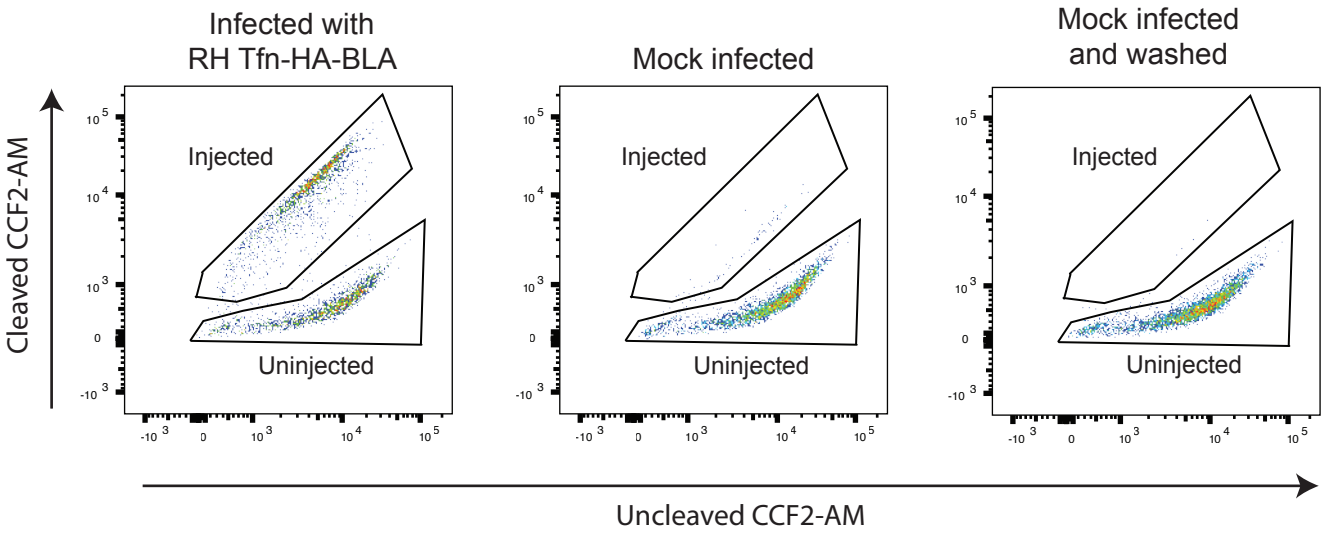

Figure S1. Human foreskin fibroblast (HFF) feeder cell debris contaminates the uninfected-injected (U-I) FACS gate. In all panels, a host cell monolayer is treated with either a parasite-free lysate of HFFs or RH Tfn-HA-BLA parasites syringe released from HFFs and then incubated with CCF2-AM to reveal (un)injected cells. *Left:* Infection with RH Tfn-HA-BLA reveals uninjected and injected cell populations. *Middle:* Mock "infection" with parasite-free lysate reveals HFF feeder cell debris contaminating the "injected" cell population. *Right:* Infection with parasite-free lysate that was washed to remove HFF debris reveals a reduction in contamination of the injected population.

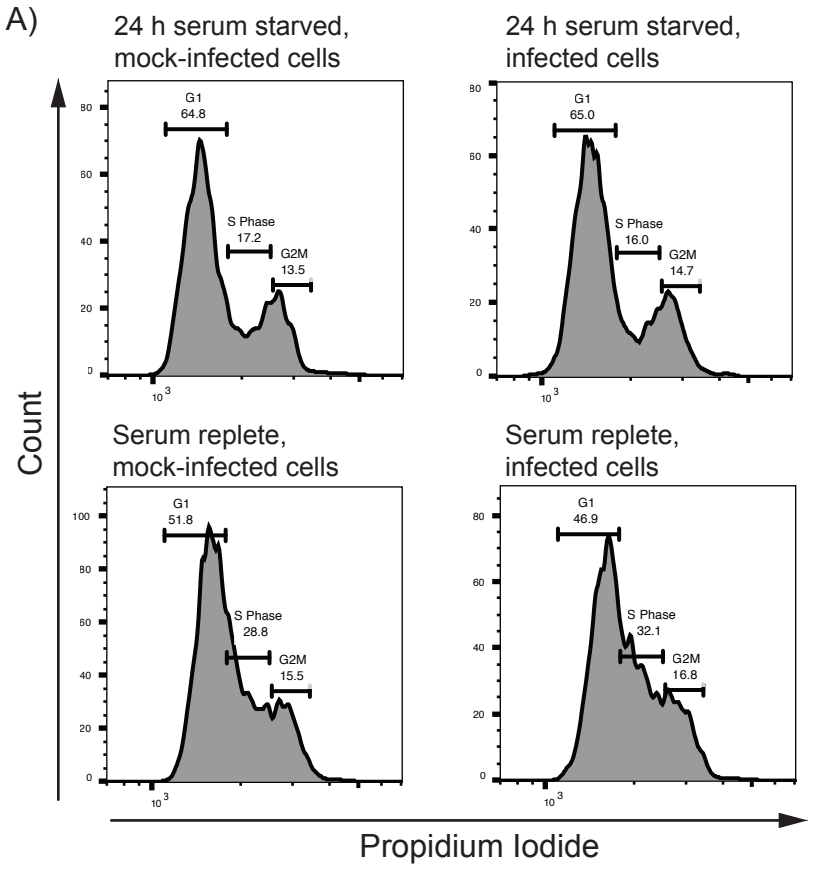

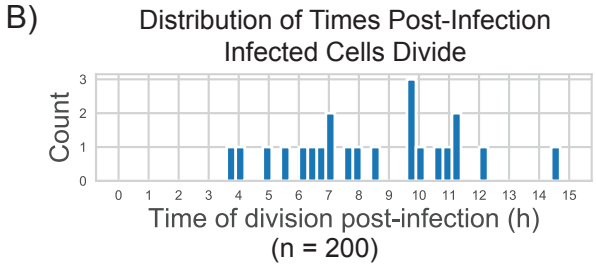

Figure S2. (A) Serum starvation for 24 h partially inhibits cell division of 10 T1/2 host cells, reducing the possibility of capturing U-I cells that arise from division of an infected host cell (U-Id cells) rather than from an aborted invasion event. Note that the S phase population in the bottom right panel (serum replete, infected cells) also contains G1 phase cells containing parasites, as parasite nuclear content enhances the propidium iodide signal in these cells. **(B)** Histogram depicting the number of infected host cells that divided at various times post-infection, as determined by live video microscopy footage of 200 serum starved 10 T1/2 cells for which the precise moment of infection was captured on camera. Of the 200 infected 10 T1/2 cells, 53 divided over a 16 hour time course, and none divided at earlier than 3.67 hours post-infection.

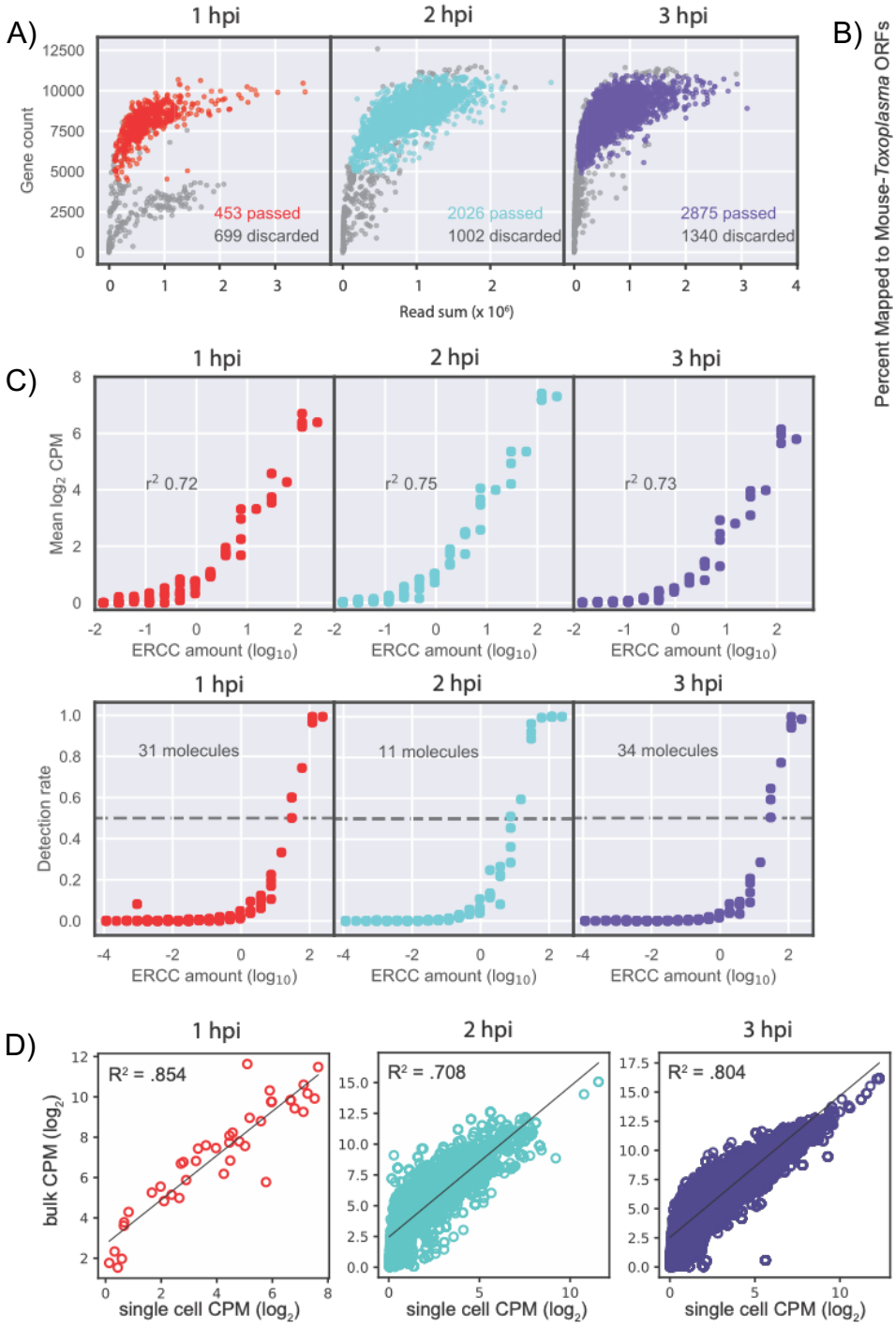

E)

	Bulk 1 hpi	Bulk 2 hpi	Bulk 3 hpi
Single Cell 1 hpi	0.854	0.655	0.630
Single Cell 2 hpi	0.742	0.708	0.788
Single Cell 3 hpi	0.669	0.621	0.804

Figure S3. Quality control metrics for single cell RNA sequencing data. **(A)** Comparison of gene counts (number of genes for which reads from each cell mapped to the concatenated mouse-*Toxoplasma* genome, y-axis) and read sum (total reads, x-axis) for all experimental trials. Cells that passed quality control are indicated in color. **(B)** Percentages of total reads that mapped to open reading frames (ORFs) in the mouse-*Toxoplasma* concatenated genome. **(C)** *Top panel:* Linear regression modeling of measurement accuracy fitted on ERCC spike-ins with abundance above the detection limit. The text within each subplot denotes the coefficient of determination for the regression fit. *Bottom panel:* Logistic regression modeling of detection limit based on ERCC spike-ins. The 50% detection rate is indicated with a black dotted line, and the text within each subplot indicates the detection limit for each experiment in absolute molecular counts. **(D)** Linear regression fitted to scatterplot of average gene counts of differentially expressed genes for single cell RNA sequencing data (x-axis) vs. bulk RNA sequencing data (y-axis). Each point represents a DEG. Text within each subplot denotes the coefficient of determination (R^2) for the regression. **(E)** The coefficients of determination for linear regression lines fit to scatterplots as in (D) for all possible combinations of single vs. bulk RNAseq combinations.

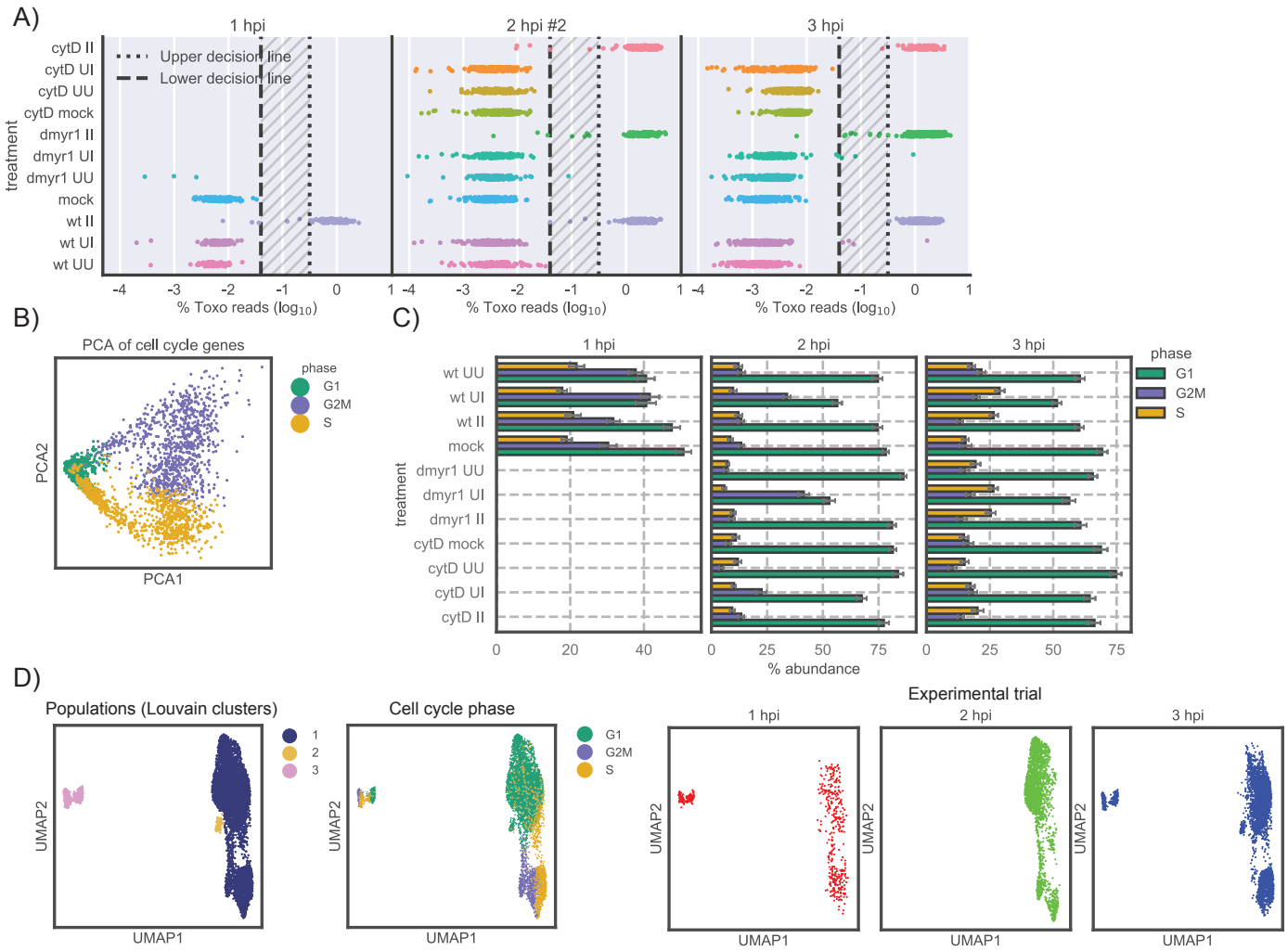

Figure S4. Single cell resolution enables strategic partitioning of individual cells for downstream analysis. **(A)** Percentage of reads derived from *Toxoplasma* validates infection status of individual cells. Cells are scored as uninfected if left of the lower decision line (bold, dashed), infected if right of the upper decision line (dotted), and ambiguous if between the decision lines (cross-hatched section). **(B)** Principal component analysis (PCA) projection of cells based on 175 curated cell cycle markers and subsequent Leiden clustering enables partitioning of cells by predicted cell cycle states, G1 (green), S (gold), and G2/M (purple). **(C)** Proportion of cells from each experimental condition in each cell cycle phase. **(D)** Dimensionality reduction and projection of single cells using the *Uniform Manifold Approximation and Projection* (UMAP) algorithm reveals 3 putative cell populations. All panels are reproduced copies of the same projection, each of which is color coded by specific parameters. *Left:* Louvain clusters, used to assign the cells to populations 1, 2, and 3; *middle:* cell cycle phase; *right (3 panels):* experimental trial (1 hpi, 2 hpi, and 3 hpi).

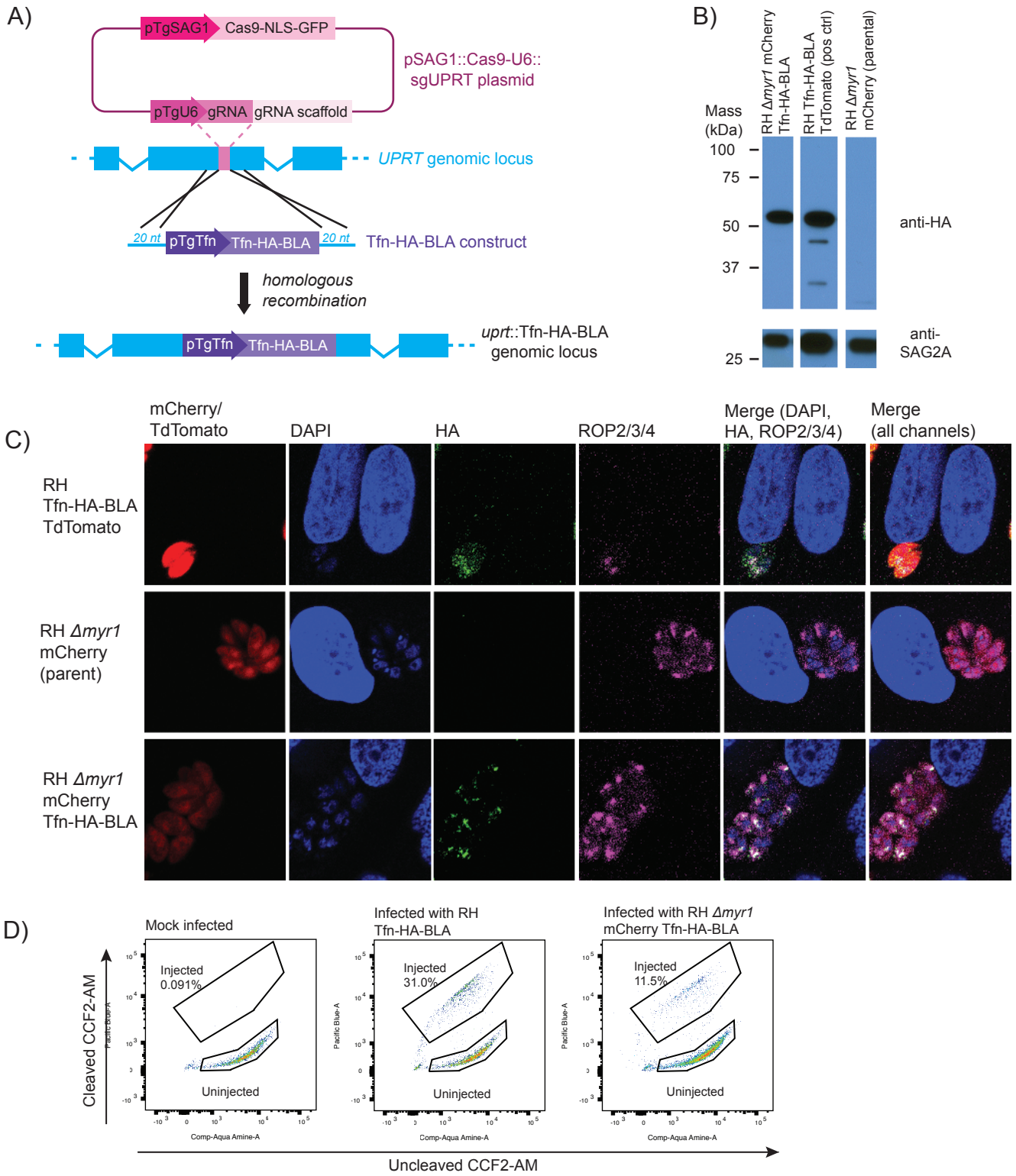

Figure S5. Construction and validation of RH *Δmyr1* mCherry Toxofilin-HA-beta-lactamase (RH *Δmyr1* mCherry Tfn-HA-BLA). **(A)** CRISPR/Cas9 strategy to construct RH *Δmyr1* mCherry Tfn-HA-BLA by disrupting parasite UPRT (blue) in parental strain RH *Δmyr1* mCherry. The parental strain was transfected with plasmid pSAG1::-Cas9-U6::sgUPRT (pink) and a linear amplicon containing Tfn-HA-BLA (purple) and flanked with 20 nucleotide homology arms to UPRT (blue). The region of UPRT complementary to the guide RNA, which also contains the site at which Cas9 cleaves, is in pink. **(B)** Western blot for the Tfn-HA-BLA construct in RH *Δmyr1* mCherry Tfn-HA-BLA. All lanes were obtained from the same gel. **(C)** Immunofluorescence assay (IFA) for colocalization of the Tfn-HA-BLA protein product and ROP2/3/4. **(D)** FACS analysis of 10 T1/2 cells infected with parasite-free lysate, RH Tfn-HA-BLA, and RH *Δmyr1* mCherry Tfn-HA-BLA. Cleavage of reporter dye CCF2-AM indicates injection of the Tfn-HA-BLA construct.

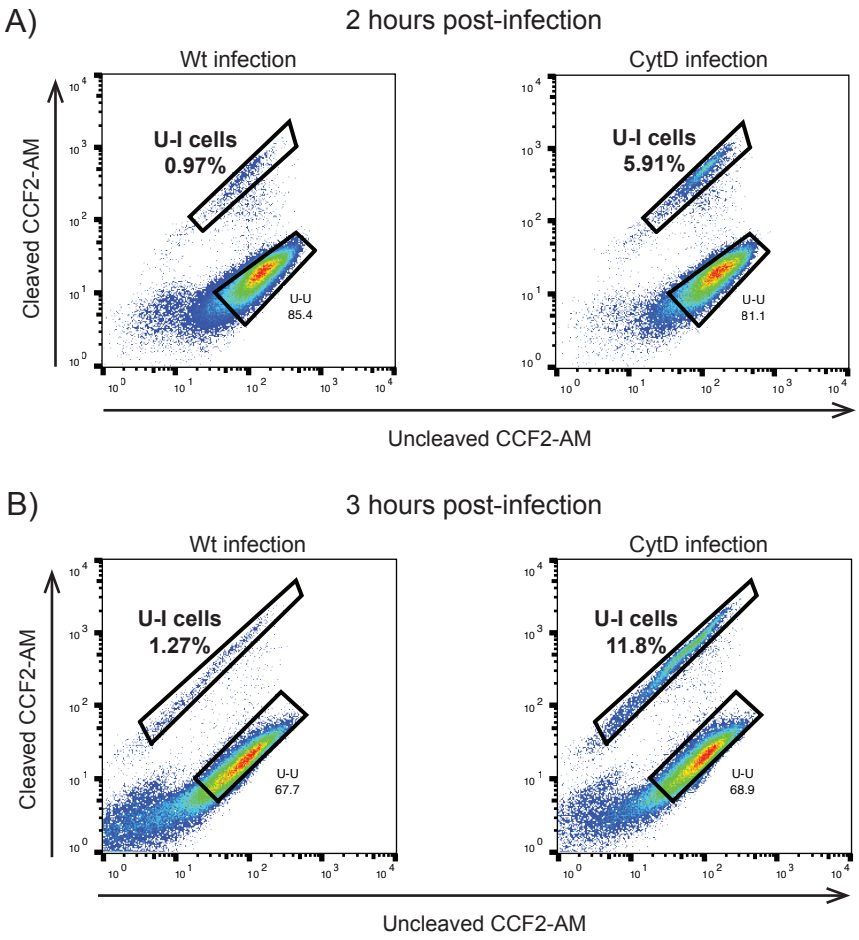

Figure S6. Effect of cytochalasin D treatment on the proportion of 10 T1/2 host cells that are U-I cells. **(A)** U-U and U-I cells that arise from Wt and CytD infections at 2 hpi. **(B)** U-U and U-I cells that arise from Wt and CytD infections at 3 hpi.